

# Influence of light, temperature and iron oxidation state on the dissolution rate of combusted iron particles in oxalic acid

M. Lausch<sup>a,\*</sup>, Y. Ruan<sup>a</sup>, P. Brockmann<sup>a</sup>, A. Zimina<sup>d,e</sup>, B.J.M. Etzold<sup>b,c</sup>, J. Hussong<sup>a</sup>

<sup>a</sup>*Technische Universität Darmstadt, Institute for Fluid Mechanics and Aerodynamics; 64347 Griesheim*

<sup>b</sup>*Technische Universität Darmstadt, Ernst-Berl-Institute for Technical Chemistry and Macromolecular Science; 64287 Darmstadt, Germany.*

<sup>c</sup>*Friedrich-Alexander-Universität Erlangen-Nürnberg, Power-To-X Technologies; 90762 Fürth, Germany.*

<sup>d</sup>*Karlsruhe Institute for Technology, Institute of Catalysis Research and Technology; 76344 Eggenstein-Leopoldshafen, Germany*

<sup>e</sup>*Karlsruhe Institute for Technology, Institute for Chemical Technology and Polymer Chemistry; 76131 Karlsruhe, Germany*

<sup>f</sup>*Technische Universität Darmstadt, Institute for Catalysts and Electrocatalysts; 64287 Darmstadt, Germany.*

---

## Abstract

In this study, the influence of temperature (40–80 °C) and light exposure on the dissolution of combusted iron particles in aqueous oxalic acid (0.45 mol/L) is experimentally investigated. Unlike previous studies, real combusted iron particles with varying fuel-to-air equivalence ratios were used instead of model oxides. In-situ video recordings reveal the evolution of particle size and morphology. Increasing temperature and short-wavelength light exposure enhance the reaction rate, with light-induced effects only becoming significant above 40 °C for the duration of the experiments. This behavior differs significantly from hematite/maghemite oxides, attributed to the internal Fe phase structure of the combusted iron particles. At 80 °C with additional light irradiation, a sudden decrease in reaction rate is observed due to solid ferrous oxide formation. While the fuel-to-air ratio induces differences in iron oxide phase composition, it does not affect the dissolution combusted iron particles significantly.

*Keywords:* iron oxide, oxalic acid, dissolution, particle morphology, metal fuel, combusted iron particles

---

## 1. Introduction

The reaction of iron oxides with oxalic acid is of significant importance in both the general bioavailability of iron [1–3] and specific industrial applications like the removal of corrosion products [4, 5] and refining ceramics [6, 7]. Oxalic acid (OxA) may offer benefits as a leaching agent in electrowinning for a carbon-free steelmaking processes. Over 80% of the energy needed to make steel is derived from fossil fuels, 75% of which is coal-based [8]. As a result, the steel industry is a significant contributor to CO<sub>2</sub> emissions, which will continue to be a concern for many years ahead. Electrowinning, along with other processes such as smelting [9] or electric arc furnaces [10, 11], could substantially reduce future carbon emissions, particularly given the current high steel production levels (reaching 1.9 Gt in 2023 [12]). Furthermore, electrowinning presents synergies with a metal fuel economy, where energy is released through combustion and then stored via the reduction of iron oxides back to iron [13–17].

### 1.1. Occurring reaction mechanisms

The dissolution of iron oxides in OxA can proceed via two pathways [18, 19], distinguished by the reduction of the iron in the crystal prior to solubilization. Numerous factors influence the contribution of the two pathways to the overall dissolution through the related reaction mechanisms and formed iron-oxalate complexes, including temperature, pH,

---

\*Corresponding author

Email address: lausch@sla.tu-darmstadt.de (M. Lausch)

light exposure and added ferrous ions in solution [1, 18–23]. Recently [24], a detailed overview has been provided regarding the interplay between those influencing factors and the current understanding of the occurring reaction mechanisms during the dissolution. Accordingly, in this section only a concise schematic overview of the proposed mechanisms is illustrated in Fig. 1. The associated equations and references can be found in Appendix A. In general, the dissolution is assumed surface-reaction controlled [18, 23, 25, 26] and thus depends only on the reaction kinetics and the available surface area. The dissolution rate per surface area is consequently independent of particle size. This assumption may become invalid for particles at the nanometer scale, where the anisotropy of the terminally coordinated Fe ions [27], the connection between single crystal faces [28, 29] due to the semiconducting properties of iron oxides and finally the increasing band gap with decreasing size [30] becomes more important. Noteworthy is the formation of solid iron oxalate dihydrate, ( $\text{Fe}^{\text{II}}\text{C}_2\text{O}_4 \cdot 2\text{H}_2\text{O}$ ) (solubility limit in water at room temperature  $c_{\text{FeC}_2\text{O}_4} \approx 447.2 \mu\text{mol/l}$  [31, p.487]), which is an unwelcome byproduct that binds some of the iron and would need to be converted to Fe e.g. through pyrolytic reduction as proposed by Santawaja et al. [32].

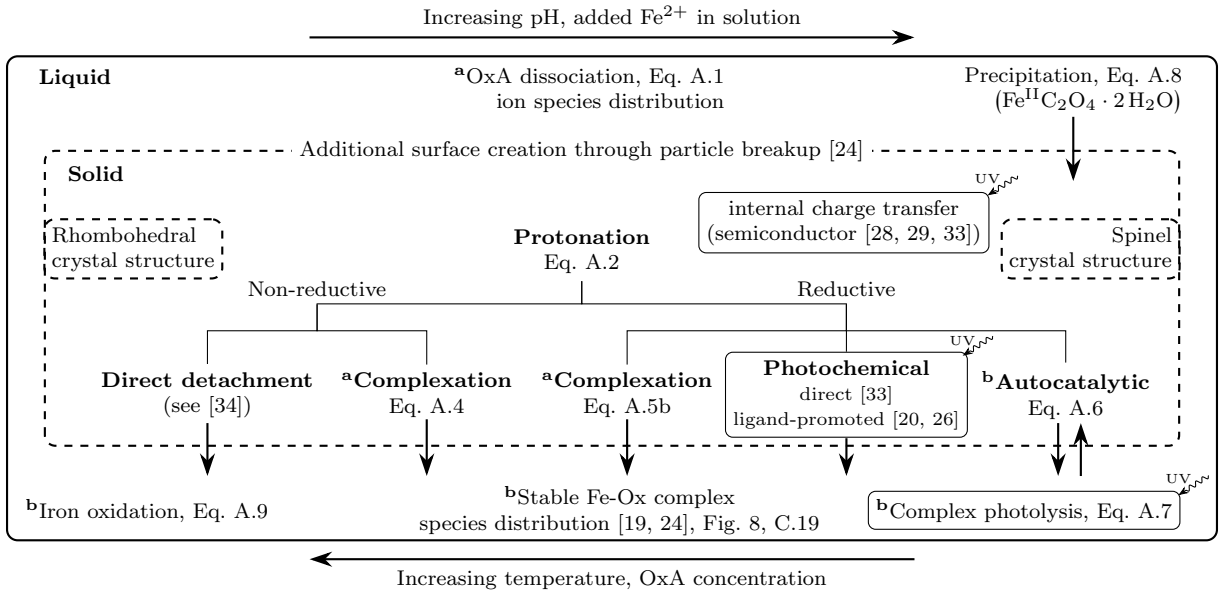


Figure 1: Schematic overview of the occurring reaction mechanisms and influencing factors. The lateral position indicates the associated dominant process (left - non-reductive; right - reductive). After protonation, all subsequent mechanisms can operate concurrently. The oxidation number of a lattice ion is represented using Roman numerals, while Arabic numerals are used for all other forms.

Besides the indicated external factors in Fig. 1, the internal properties of the particles also shift the balance of occurring mechanisms. If the crystal contains  $\text{Fe}^{\text{II}}$ , as for magnetite or wüstite, the autocatalytic mechanism is already active in the beginning of the reaction, resulting in faster dissolution [18, 35, 36]. Independent of the formal oxidation state, the crystal structure results in an increased dissolution rate for spinel-phase maghemite ( $\gamma\text{-Fe}_2\text{O}_3$ ) relative to rhombohedral hematite ( $\alpha\text{-Fe}_2\text{O}_3$ ) [18]. As demonstrated recently [37] for suppressed autocatalysis at 0.5 mol/l OxA concentration, the crystal structure determines primarily if the reaction proceeds predominantly reductively or non-reductively. If the particles are suspended by a stirrer, the fluid shear rate and interactions with both the wall and other particles can lead to particle breakup, effectively increasing the available surface area for reaction [24, 38].

In contrast to the pure iron oxides that are typically the subject of dissolution studies in the literature, the structure of industrially relevant combusted iron particles (CIPs) differs substantially in both macroscopic and microscopic features. In view of the important interactions between particle characteristics and dissolution processes, a brief overview of the current findings on the combustion process, structure and composition of CIPs is presented.

## 1.2. Composition of combusted iron particles

The majority of CIPs are spherical with gas-filled cavities, occasionally displaying cracks and grooves across the surface [39–43]. Attili et al. [44] noticed also significant swelling of the particles during their laser-induced single particle combustion experiments, which could be related to the gas production during combustion [45]. As shown by Choisez et al. [42] CIPs (without propane-assistance) are composed of a thin hematite shell surrounding a perforated core of magnetite interspersed with hematite spikes. For the CIPs of diameters greater than 40  $\mu\text{m}$ , the morphology of the particles resembles a hollow sphere with a thin oxide shell [46]. During the combustion process, the particle size and temperature determine if either external diffusion, internal diffusion or kinetics limit the reaction of the particles [47]. For smaller particles with diameters assumed below 5  $\mu\text{m}$  [48–51], the reaction is kinetically controlled, while bigger particles are limited by diffusion [52]. Ning et al. [51] conducted single particle combustion experiments (diameter 20–65  $\mu\text{m}$ ). They argue based on the scaling of the particle diameter with burn time that the process transitions from externally to internally limited diffusion, once the oxygen solubility limit is reached on the particle surface, comparable to Zirconium particle combustion [53]. However, Mi et al. [47] assume that the internal diffusion is instead of oxygen anions limited by the Fe cations during the gradual inward formation of  $\text{Fe}_3\text{O}_4$  inside the melted FeO droplet. The  $\text{Fe}_3\text{O}_4$  layer is subsequently further oxidized by the formation of a  $\text{Fe}_2\text{O}_3$  shell. The growth rate of the shell is governed by the combined diffusive limit of Fe cations and oxygen anions and assumed a function of the ambient oxygen concentration [47]. Thus, the surrounding oxygen concentration directly influences the ratio of hematite to magnetite in the particles. This composition may also depend on the cooling rate of the particles after the combustion [51], which suggests that it depends on the geometry of the burner. The particles used in the present study are collected after combustion in iron powder-air flames in a tube burner [54]. They mostly comprise hematite and magnetite with traces of  $\alpha$ -Fe and FeO and covered in oxide nanoparticles [55]. While there is no analysis of the Fe phase for the nanoparticles for this powder, the nanoparticles found in the fumes during the combustion of sponge iron were shown to consist mainly of maghemite ( $\gamma$ - $\text{Fe}_2\text{O}_3$ ) [39]. The rate of nanoparticle production during combustion was shown to increase with decreasing fuel-to-air equivalence ratio,  $\Phi$  [45, 56]. Decreasing  $\Phi$  also results in a higher degree of oxidation with an increase in the fraction of hematite and corresponding decrease in magnetite, wüstite and ferric iron [42, 55]. Uncombusted iron can be embedded inside the oxide particles or may exist as a separate particle [37, 57].

Previous studies have investigated the dissolution for pure, reference oxides [18, 21, 23, 34]. However in the case of CIP dissolution, the interplay is further complicated by anisotropic particle properties, such as their hollow structure and layered composition of different iron oxides. As the particles dissolve, this exposes surfaces with different characteristics to the acid and thus shifts the balance of governing mechanisms. The effects of mixed phases on dissolution processes have not been as extensively studied as those of pure iron oxides as mentioned recently [37], primarily appearing in research involving the purification of clay materials such as kaolin [6, 7, 58, 59] or rust removal [60]. The addition of  $\text{Fe}^{2+}$  may also speed up the reaction process through activation of the autocatalytic pathway, either through the addition of a salt [7, 59] or via  $\text{Fe}^{\text{II}}$ -containing oxides like magnetite [58]. While these are examples of mixed phases reacting at the same time, comprehensive insights into the processes taking place for individual mixed-phase particles remain insufficiently developed. The dissolution mechanisms of CIPs in OxA at approximately 60°C, with a suppressed autocatalytic pathway, were recently studied systematically [37], concluding that the rhombohedral phase (hematite) dominates the dissolution, despite the presence of magnetite in the particles. However, beyond limiting the investigated reaction mechanisms, the study was also restricted to a single set of temperature and light conditions, lacking a systematic exploration of their broader influence.

In summary, the dissolution of iron oxides is highly complex and numerous factors are interconnected in their

influence on concurrent reaction mechanisms. Nevertheless, in context of electrowinning there is a clear requirement for further investigation into the dissolution of CIPs, along with a systematic variation of boundary conditions. Consequently, the objective of this study is to examine the dissolution of CIPs in a batch reactor in aqueous oxalic acid, with a systematic variation of temperature, fuel-to-air equivalence ratio and light exposure.

## 2. Materials and Methods

### 2.1. Chemicals

Combusted iron particles were obtained from iron powder-air flames in a tube burner at a constant mean outlet velocity of 35 cm/s [54] with three different fuel-to-air equivalence ratios  $\Phi$  of 0.67, 1.0 and 1.5 (assuming full conversion to  $\text{Fe}_2\text{O}_3$  for calculation). Similar to a previous study [24], the particles are then used to prepare a 2.5 g/l stock solution of the respective iron oxide. A stock solution of 5,wt% Pluronic F127, a nonionic surfactant (Merck, Germany), was prepared to inhibit the agglomeration of hydrophobic particles and their adhesion to the walls of the reaction vessel. Bidistilled water (CarlRoth, Germany) was employed in the preparation of all stock solutions. OxA was sourced from a 0.5 mol/l stock solution (Chem-Lab, Belgium). The reaction was initiated by the addition of 15  $\mu\text{l}$  of Pluronic F127 solution into the cuvette, corresponding to approximately 0.25 wt%, followed by 35  $\mu\text{l}$  of bidistilled water, 2.25 ml of OxA stock solution, and finally 200  $\mu\text{l}$  of iron oxide suspension. This preparation yielded a total cuvette volume of 2.5 ml. The resulting OxA concentration is  $c_{\text{H}_2\text{C}_2\text{O}_4} = 0.45 \text{ mol/l}$ .

### 2.2. Experimental setup and methodology

To estimate the influence of reaction temperature  $\bar{T}$ , light irradiation and fuel-to-air equivalence ratio  $\Phi$  on the dissolution rate of the CIPs in 0.45 mol/l OxA, a pre-existing experimental setup is utilized [24]. The setup consists of a fused-silica macro cuvette in which a rotating cylinder keeps the particles suspended. The cuvette is preheated to the desired temperature using a water jacket and the preparation of the cuvette is described in Sec. 2.1.

An experiment begins ( $t = 0$ ) with adding the CIPs to the solution, immediately starting the cylinder rotation and simultaneously activating the camera image acquisition. An experiment is considered completed if either no particles can be detected anymore (optical resolution limit set at 5  $\mu\text{m}$  particle diameter) or the reaction reaches a duration of 10 h. The cylinder is then cleaned in an ultrasonic water bath for 3 min and subsequently rinsed with bidistilled water. After the cuvette is cleaned with bidistilled water, the hydrophobic coating at the top edges is renewed, thus concluding the experimental procedure.

The setup is equipped with a video system to obtain temporarily resolved *in-situ* data of the particles during the dissolution. Post-processing of the data yields the projected area  $A$  of each detected particle as well as the Feret diameter ratio  $F = F_{\text{max}}/F_{\text{min}}$  (where a F-value of one corresponds to a circle and higher values to needle-shaped objects) at different boundary conditions. These geometrical descriptors can be found in Fig. 2. The values of  $A$  in the recorded images of all particles are then used to calculate the area-equivalent particle diameter  $d = \sqrt{4A/\pi}$ . Using the total number of all particles  $n$  in one of the 60 discrete time intervals is then used to estimate the median particle diameter  $\tilde{d}$ . A bootstrap procedure with 4000 bootstrap samples yields an estimation of the 95% confidence interval of the non-normal distribution  $\tilde{d}_{95,\text{boot}}$  in each time interval [24].

The discrete values (levels) of the controlled parameters (factors) are chosen such that they are consistent with previous experiments and a significant effect size is expected, defined as the difference between the mean level values per variance [61]. The equidistant level value distribution also complies with a full factorial design, which allows to determine the significance of each factor and to resolve interactions between the factors without confounding. To determine the significance of one factor, first the mean of each level is calculated using all experimental runs with

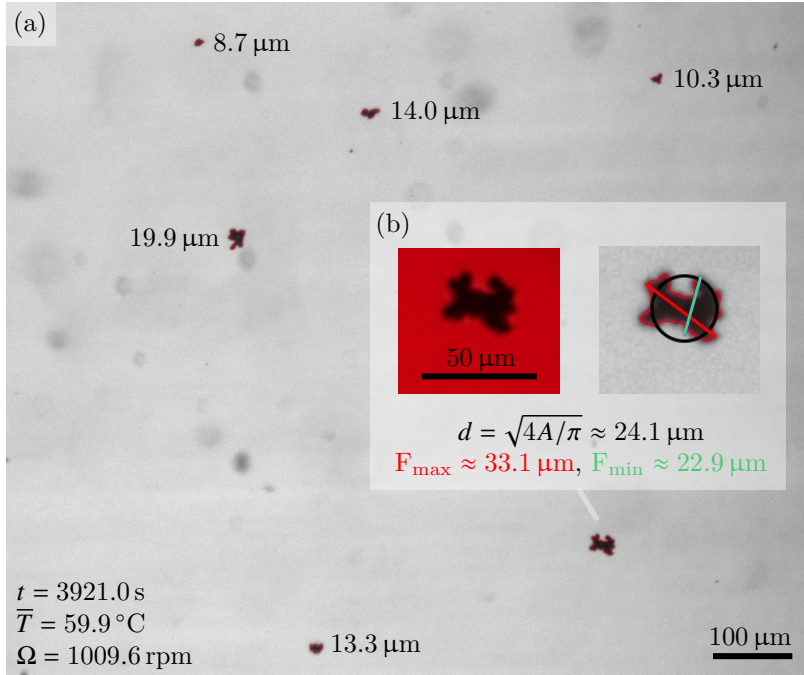


Figure 2: (a) Example image taken from an experimental run ( $\Phi = 1.0$ ,  $\bar{T} = 60^\circ\text{C}$ , with light) approx. 65 min after reaction begin. Red contour lines indicate the detected object perimeter, the number next to each object denote the area-equivalent particle diameter  $d$ . (b) Unprocessed image and the corresponding processed image of an exemplary detected object. Indicated are the black area-equivalent circle at the centroid of the object and the minimum and maximum Feret diameter in green and red (FR  $\approx 1.45$ ).

that level value, irrespective of the other factor level values. Due to the symmetric level value distribution of the experimental runs, the influence of all other factors levels on the mean is eliminated (orthogonality). For a single factor and two level values, the significance can then be determined using a simple two-sample t-test. For the present case of three systematically varied parameters, a 3-way analysis of variance (ANOVA) is performed. The discrete values of the parameters used in this study are summarized in Tb. 1.

Controlled parameters	Level 1	Level 2	Level 3
Stirring speed in rpm	1000		
Particle loading in g/l	0.2		
OxA concentration $c_{\text{H}_2\text{C}_2\text{O}_4}$ in mol/l	0.45		
Light irradiation wavelength in nm	640 (peak)	640 + 190-2500 (broadband)	
Fuel-to-air equivalence ratio $\Phi$ of CIPs	0.67	1.0	1.5
Reaction temperature $\bar{T}$ in $^\circ\text{C}$	40	60	80

Table 1: Mean values of experimental parameters varied during experiments. For convenience the light irradiation level values are denoted *no light* (**Level 1**) and *light* (**Level 2**) in the manuscript.

There are 18 possible combinations for this set of parameters. Each combination of parameters was repeated two times, resulting in a total of 36 experimental runs. In addition three experiments at approx.  $25^\circ\text{C}$  without broadband light are performed. Despite the best efforts to set  $\bar{T}$  exactly at the specified level values, there are slight variations of approx.  $\pm 0.35\text{K}$  with the maximum deviation for one experimental run of  $1.5\text{K}$  from the target temperature. The exact values can be seen e.g. in Fig. 7. Thus, the factors  $\Phi$  and light irradiation are treated categorically and  $\bar{T}$  is assumed as continuous variable. However, treating  $\bar{T}$  also categorically does not change the outcome of the statistical analysis in Sec. 3.1.

### 3. Results and Discussion

The evolution of the median particle diameter for all combinations of temperature, light irradiation and fuel-to-air equivalence ratio is shown in Fig. 3. As the particles dissolve, their average size decreases, as can be seen from the

evolution of  $\tilde{d}(t)$ . In the beginning of an experiment,  $\tilde{d}$  and maximum  $\tilde{d}_{\max}$  varies between approx.  $7.5 \mu\text{m}$  and  $9.7 \mu\text{m}$ . In agreement with the literature [37, 55],  $\tilde{d}_{\max}$  increases slightly with increasing  $\Phi$  from approx.  $8.1 \mu\text{m}$  ( $\Phi = 0.67$ ),  $8.3 \mu\text{m}$  ( $\Phi = 1.0$ ) to  $8.5 \mu\text{m}$  ( $\Phi = 1.5$ ). However, as shown in Fig. B.18, the scatter in the data is high and a subsequent one-way ANOVA revealed that this trend is actually insignificant at the significance level  $\alpha = 5\%$ . Changing the boundary conditions specified in Tb. 1 results in different dissolution rates. In this section, first the overarching trends and significant parameters for the dissolution are identified, followed by a discussion of the observed shift in particle morphology. Subsequently, a detailed investigation of the influence and interaction of the significant factors is presented and recommendations for optimizing future dissolution processes are given.

### 3.1. Variance analysis of the influencing parameters

To identify the significant influencing parameters for the dissolution process, the rate of change in particle size is first calculated. Subsequently, the significance of the factors outlined in Table 1 is evaluated using an 3-way ANOVA. For most CIP dissolution experiments,  $d\tilde{d}/dt$  remains almost constant. However, on closer inspection of the data presented in Fig. 3, it becomes clear that actually most experimental runs exhibit a deviation from the linear trend in the beginning. This can be attributed in part to the gradual suspension of the particles as the cylinder spins up in the beginning of an experiment and the breakup of clusters, discussed in detail in Sec. 3.2. The influence of the gradual suspension is expected to be higher for experiments of shorter duration, as there is less elapsed time per interval. Aside from these initial fluctuations, a distinct change in rate can be observed towards the end of some experimental runs, particularly at higher temperatures (Fig. 3 (a), (b)). The evolution of  $\tilde{d}(t)$  contrasts with those observed with the mixed-phase  $\text{Fe}_2\text{O}_3$  particles [24]. In the latter case, a distinct change in rate in the beginning of an experiment was attributed to the shift from breakup-dominated to the dissolution-dominated phase in the experiment.

To determine the dissolution rate from the data presented in Fig. 3, the values  $\tilde{d}(t)$  are linearly fitted using a iterative robust procedure based on the Huber loss function (MATLAB fitlm) [62]. The weights are taken as the inverse variance derived from the  $\tilde{d}_{95,\text{boot}}(t)$  values. This way, both outliers and  $\tilde{d}(t)$  values with higher uncertainty are contributing less to the fit. To account for the change in rate observed in some of the experimental runs, the experimental data is split into two segments based on the inflection point of the first derivative. Thus, for certain experimental runs with segmented data, two rate values are obtained, denoted as  $c_1$  and  $c_2$ , respectively. In the following statistical analysis, only the initial rate is used. However, for the detailed discussion of the influence of temperature and light on the dissolution process in Sec. 3.3, both the first and second rate are considered.

The fit shown in Fig. 4(a) gives an example for the non-segmented experimental data. While most  $\tilde{d}$  values follow the linear trend closely, there is a deviation for the initial  $\tilde{d}(t \approx 13.7 \text{ min})$ , where the influence of initial particle suspension is suspected to be greatest. Fig. 4(b) shows a representative fit for segmented data. In this case  $\tilde{d}(t)$  deviates from the ideal linear evolution, reflected in a greater 95% confidence interval (CI) of the fit. While it would be tempting to use higher order polynomial to fit these experimental runs, in our tests some of these models still not fit the data well, suggesting that the increased complexity does not necessarily yield a better model. Thus, a simple first order polynomial is deemed more appropriate for the data presented in Fig. 4(b). The inaccuracies introduced by using a linear fit are mitigated by the inclusion of the 95% CI of the fit parameters in the analysis.

The rates  $c_1$  extracted from the fitting procedure are used in a next step to determine the significant factors. Significance of an effect or an interaction effect on measured response is determined by performing an ANOVA with the null hypothesis to disprove that there is no effect on  $c_1$  at the  $\alpha = 5\%$  threshold. The ANOVA requires mutual independence, normal distribution and equal variances of the error variable for any inference drawn to be

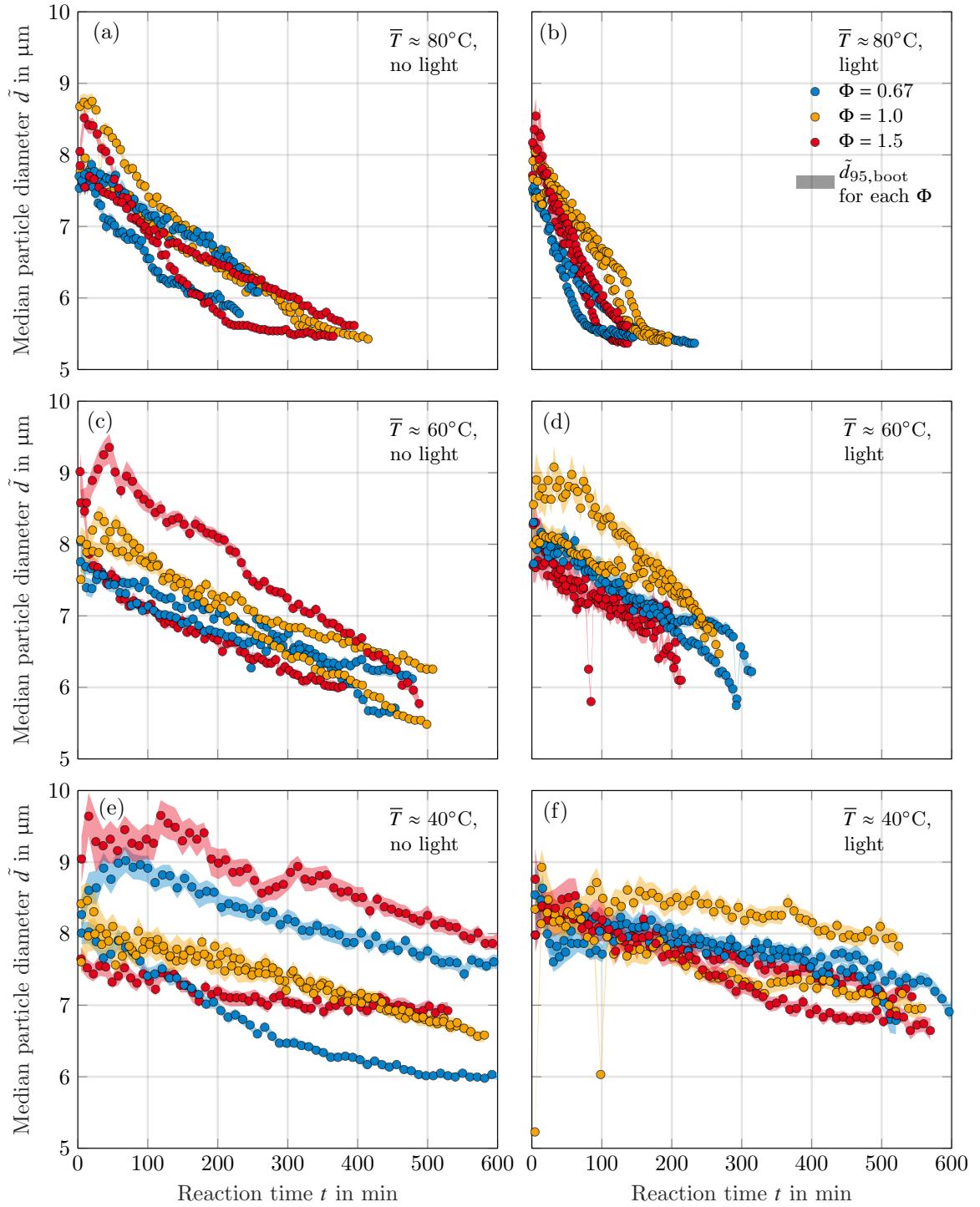


Figure 3: Median particle diameter  $\tilde{d}(t)$  at  $\bar{T} = 40^\circ\text{C}$  (a,b),  $60^\circ\text{C}$  (c,d) and  $80^\circ\text{C}$  (e,f), both with (a,c,e) and without (b,d,f) light irradiation for varying  $\Phi$  (0.67, 1.0, 1.5), each measured two times.

valid. Besides the inspection of factor level variance, this can be tested by scrutinizing the standardized residuals. Standardized residuals are obtained by calculating the difference between measured  $c_1$  and predicted ANOVA model value for that factor level combination divided by its estimated standard deviation [63, pp. 143-144]. As described in Sec. Appendix B in more detail, the violation of some of the requirements necessitated a data transformation. The subsequently obtained ANOVA model for the transformed rate,  $\Xi$ , includes insignificant terms, which must be excluded systematically. This is achieved through an adjusted backward elimination procedure in which iteratively the term with the highest p-value (most insignificant) is excluded and the ANOVA results recalculated using the reduced model. After each step it is checked if a re-introduction of any excluded model term would result in its p-value below the  $\alpha = 5\%$  threshold. If that criterion is met, the term is included in the next model step and the

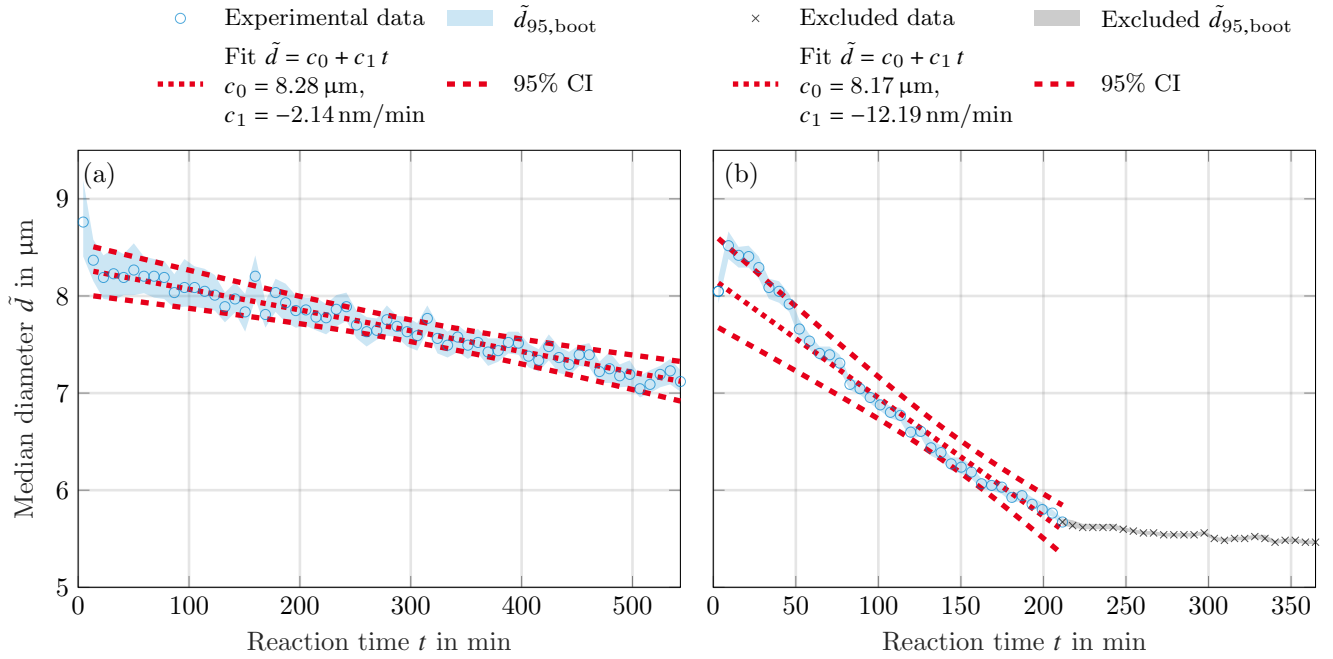


Figure 4: (a) Linear fit for the factor combination  $\bar{T} \approx 40.0^\circ\text{C}$ , light,  $\Phi = 0.67$ , with 95%  $\text{CI}(c_0) = [8.1, 8.5] \mu\text{m}$ ,  $\text{CI}(c_1) = [1.5, 2.7] \text{ nm/min}$ . (b) Segmented linear fit for the factor combination  $\bar{T} \approx 80.2^\circ\text{C}$ , no light,  $\Phi = 0.67$ , with 95%  $\text{CI}(c_0) = [7.8, 8.5] \mu\text{m}$ ,  $\text{CI}(c_1) = [9.8, 14.6] \text{ nm/min}$ .

ANOVA computed again. After completion of the procedure only significant terms remain in the model and the standardized residuals are again inspected. Normality, homoscedasticity and independence are all deemed suitably met, as shown in Fig. B.13, B.14 and B.15. The significance of each term in the initial and the reduced ANOVA model is graphically represented in Fig. 5 in blue and red, respectively. The null hypothesis is rejected and an effect is considered significant when the standardized effect strength represented by a t-value defined in Eq. 1 is above a threshold value associated with the global significance level taken at 5%. Note that this threshold value is dependent on the degrees of freedom of the ANOVA model and thus changes slightly depending on the number of terms included in the model. As already stated in a different context [64], the t-value in Fig. 5 is calculated as the

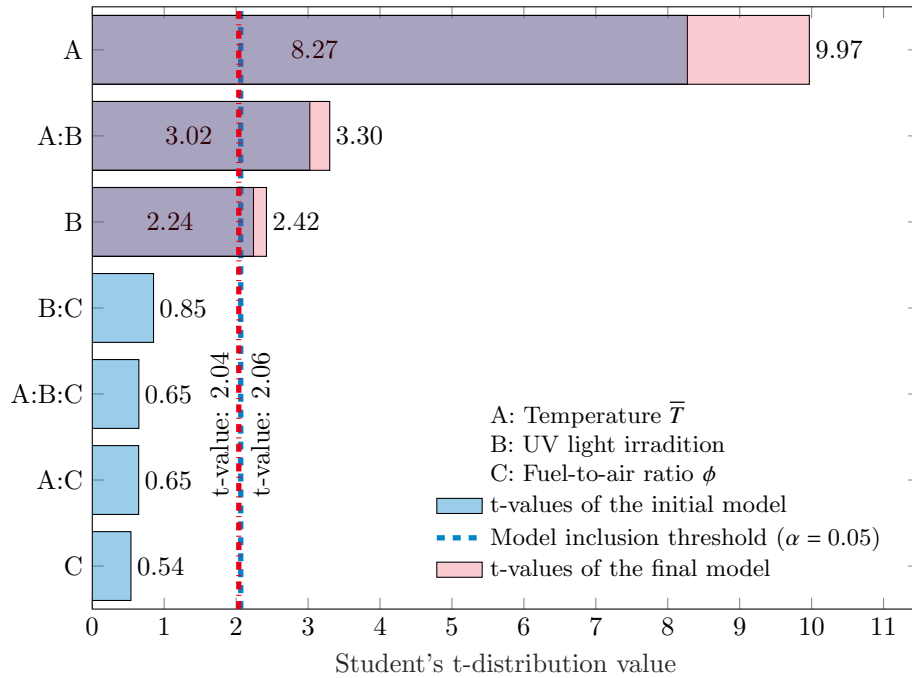


Figure 5: Graphical representation of the ANOVA results in form of a Pareto chart.

inverse Cumulative Distribution Function (CDF) of the Student's t-distribution for a given ANOVA p-value  $p_A$  as

$$\text{t-value} = F_t^{-1} \left( 1 - \frac{p_A}{2} \mid \text{DF}_E \right), \quad (1)$$

where  $F_t^{-1}$  denotes the inverse Student's t CDF and  $\text{DF}_E$  the degrees of freedom of the error. For terms with more than one degree of freedom (e.g.  $\Phi$ )  $\text{DF}_E$  equals the total degrees of freedom of the model (number of experiments minus one) minus the sum of the degrees of freedom of each included term. If a term has only one degree of freedom (e.g. light irradiation), the  $\text{DF}_E$  equals the total degrees of freedom of the model minus two, thus reverting to a simple two-sample t-test.

Besides the significant effect of  $\bar{T}$  and light, which could also be deduced from the raw data shown in Fig. 3, the ANOVA reveals an additional interaction between the factors. This means that the effect of temperature on  $c_1$  depends on the state of light irradiation. Interestingly, the results in Fig. 5 also indicate that  $\Phi$  has neither an effect on the transformed rate,  $\Xi$ , itself, nor does it participate in any significant interaction (see also Fig. B.17). This is a surprising result, considering that increasing  $\Phi$  generally leads to an increase in  $\text{Fe}^{\text{II}}$  content which in turn is expected to mainly boost the autocatalytic pathway. This result also indicates that the observed lack of influence of  $\Phi$  on the dissolution mechanisms during the X-ray absorption spectroscopy measurements [37] is representative for longer reaction times and seems unaffected by the presence of an autocatalytic pathway. This may be due to an effect size too small to detect with the current method, or it could be due to the hematite interstitials blocking access to the magnetite core. In the latter case, there could still be an influence of the ferrous ions on the dissolution process once the hematite shell has been dissolved (see Sec. 3.3). However, the influence of the increased reaction rate of the spinel-type magnetite would be suppressed, leading to smaller differences between different values of  $\Phi$ . Since it is known [37, 55] that  $\tilde{d}$  is a function of  $\Phi$  and a slight dependency has been detected also in the presented set of experiments (Fig. B.18), the potential correlation of  $\tilde{d}_{\text{max}}$  and  $\Xi$  is investigated since that could obscure a potential influence of  $\Phi$ . This influence is investigated by plotting the standardized residuals against  $\tilde{d}_{\text{max}}$ . As shown in Fig. B.16, there is no discernible trend, meaning that there is no significant influence of  $\tilde{d}_{\text{max}}$  on the statistical analysis presented in Fig. 5.

### 3.2. Particle morphology

The detected particles in the recorded images also exhibit a variety of shapes that are in general non-spherical, as evident through  $\tilde{F}\tilde{R} > 1$  in Fig. 6(a), but distinct from the  $\text{Fe}_2\text{O}_3$  particle morphology of previous experiments [24]. In general, the median  $\tilde{F}\tilde{R} \approx 1.54$  (95% CI [1.50, 1.55]) for all the experiments, that indicates elongated or irregular shaped objects. This does not agree with the scanning electron microscopy images in Fig. 6(b) of the CIPs, which clearly show that the particles are spherical consistent with reports from the literature [39–43]. This leads to the conclusion that most of the detected objects are clusters of particles rather than single, non-spherical particles, as shown in Fig. 6. However, there are also some objects with almost perfectly spherical morphology, which are likely big, single particles. The evolution of  $\tilde{F}\tilde{R}$  hints at different fragmentation mechanisms at play during the dissolution. While  $\tilde{F}\tilde{R}$  fell continuously for the  $\text{Fe}_2\text{O}_3$  particles, indicating their gradual breakup, the detected CIPs first become more needle shaped, before transitioning towards rounder shapes [24].

This could be explained by the method of preparation of the experiment. As described in Sec. 2.2, due to the small masses in the experiment the particles are suspended in water before they are introduced into the setup. Both during the SEM measurements and in preliminary experiments in water big particle clusters could be seen forming. The increase in  $\tilde{F}\tilde{R}$  could be due to the gradual elongation of the larger clusters caused by the hydrodynamic shear imposed onto the solution by the cylinder. Once the shear and breakup of the clusters has proceeded to individual

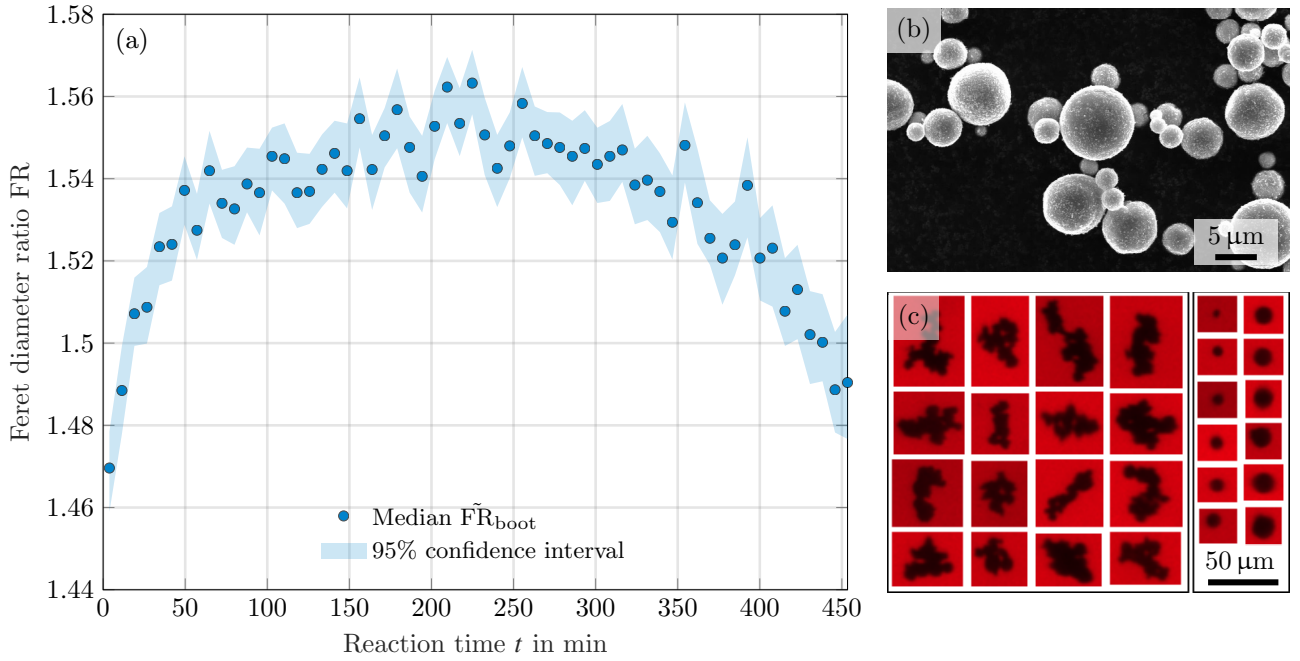


Figure 6: (a) Evolution of Feret diameter ratio for  $\bar{T} \approx 59.9^\circ\text{C}$  without light and  $\Phi = 1.5$ . The median  $\text{FR} \approx 1.54$  with a 95% CI of [1.52, 1.55]. (b) SEM images of CIPs with  $\Phi=1.5$ , taken from Lausch et al. [37]. (c) Example images of detected particles and clusters.

spherical particles, the median Feret diameter ratio decreases again. Even though the particles cluster in solution, no residue could be seen on the cuvette walls during or after an experiment, due to the use of the F127 surfactant. While the observed clustering of particles may more accurately reflect the state during the actual dissolution process as part of the electrochemical reduction, this phenomenon complicates the estimation of the dissolution state. Due to the use of optical techniques, the effects of cluster breakup and dissolution are confounded. To avoid the clustering of the particles, the concentration of the surfactant could be increased. However, in our preliminary tests this degrades the image quality due to the formation of schlieren or streaks and leads in excess to bubbles and foaming induced by the cylinder rotation. This procedure would also not prevent the clusters in the beginning of the experiment, since they are already observed in dry conditions maybe due to tribological forces during the transport or collection of the particles. The use of a surfactant during stock solution preparation would introduce an additional source of variability in the experiments since the interaction between particle and surfactant would have to be timed. An ultrasonic cleaner could destroy some of the hollow structures in the particles. Thus, to disentangle cluster breakup and particle dissolution, in a next step, the mean cluster breakup rate is estimated.

### 3.3. Influence of temperature and light on the dissolution process

In order to estimate the influence of particle breakup on  $c_1$ , the temperature is lowered further to room temperature (approx.  $25^\circ\text{C}$ ) for  $\Phi = 1.5$  without light, while the other parameters specified in Tb. 1 are kept constant. The diameter evolution is presented in Fig. D.22 in the Appendix. This adjustment aims to maintain the state of the governing inter-particle forces responsible for the formation and breakup of the clusters, including pH, ionic strength, dielectric constant of the solvent, particle concentration, and hydrodynamic shear rate. At the same time, the reported low reaction rates at temperatures below  $35^\circ\text{C}$  [35], result in a significantly reduced influence of the dissolution on  $c_1$ . As shown in Fig. 7, the rates obtained for the fixed boundary conditions at  $\bar{T} < 40^\circ\text{C}$  are statistically indistinguishable from those obtained at  $\bar{T} \approx 40^\circ\text{C}$ . This indicates that even up to  $40^\circ\text{C}$ , cluster breakup is still the dominating mechanism rather than particle dissolution. This finding is further supported by the rising number of detected particles  $n/n_0$  until the end of an experiment (see Fig. D.21). By increasing the total available surface area the cluster fragmentation is indirectly contributing to the dissolution profile [24].

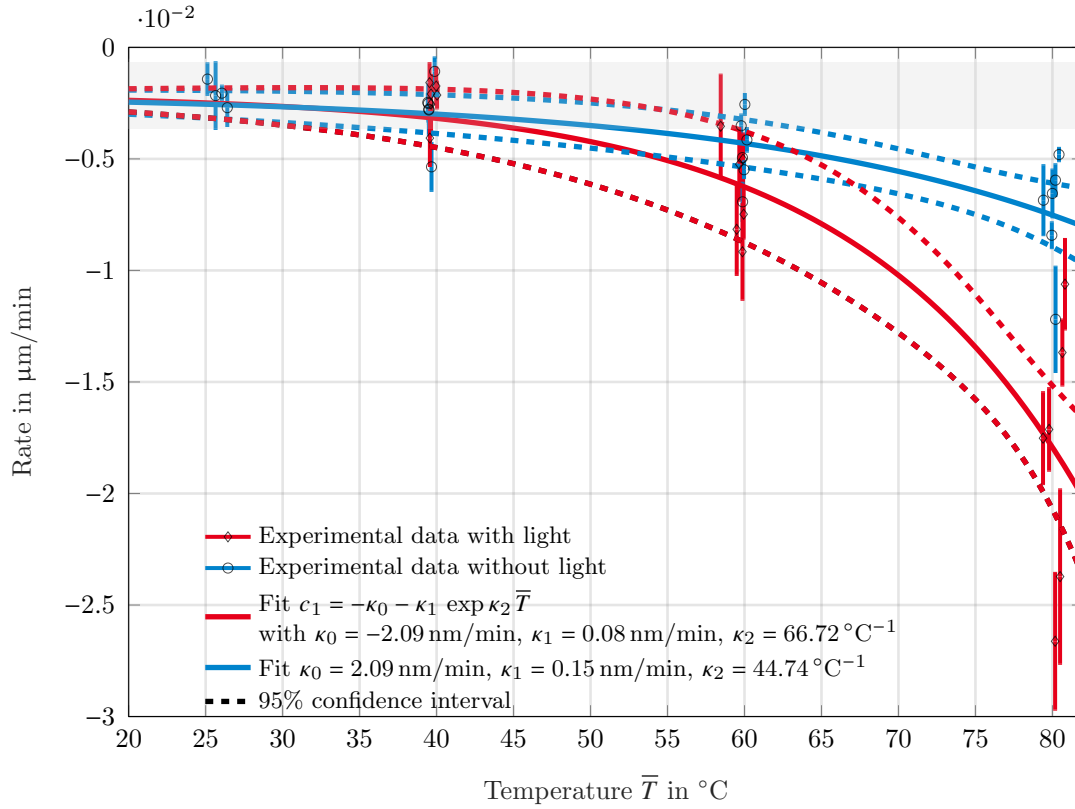


Figure 7: Estimated  $d\tilde{d}/dt$  ( $c_1$ ) as a function of temperature both with and without light, fitted by an exponential function. The gray shaded marks the minimum and maximum  $c_1$  CI value of fragmentation.

Interestingly, at 40°C light does not contribute significantly to  $c_1$ , only at higher temperatures the influence of light becomes apparent. Consequently, higher rates at higher temperatures can not be simply caused by a higher activity of the surfactant, which would be a function of temperature only. This interaction between temperature and light is a surprising result, considering that the  $\text{Fe}_2\text{O}_3$  particles dissolved faster with light at lower temperatures [24]. Even more so, the particular  $\text{Fe}_2\text{O}_3$  particles in these experiments were also a combination of rhombohedral and spinel crystal structure [37], similar to the CIPs. Considering the schematic overview of reaction mechanisms in Fig. 1, this means that in the present case the internal structure of the phases is the decisive factor rather than the bulk crystal structure. As described in Sec. 1.2, the particles are composed of a hematite shell surrounding a perforated core of magnetite interspersed with hematite spikes. At 40°C, the reaction rate associated with the hematite shell may actually be so low that the concentration of dissolved iron in solution is insufficient for the additional reduction of a few complexes to influence the dissolution rate. As the temperature increases, so does the concentration of  $\text{Fe}^{3+}$  complexes that can be reduced by light. Consequently, at 60°C, a shift towards higher rates is observed to  $c_1 \approx -0.63 \times 10^{-2} \mu\text{m}/\text{min}$ , which is significantly different from the fragmentation rate that is about  $c_1 \approx -0.29 \times 10^{-2} \mu\text{m}/\text{min}$ . This trend continues at 80°C, where the greatest difference between the rates with and without light can be observed. In general, there is a complex interplay between OxA concentration and pH on the resulting distribution of iron oxalate complexes. Additionally, increasing temperature leads to an inherent shift of pH values towards lower levels, as discussed previously [24]. An additional overview is provided in Fig. C.19 in the Appendix. From the rate data presented in Fig. 7, it can be concluded the presence of  $\text{Fe}^{2+}$  is beneficial for accelerating the dissolution process in the beginning of an experiment and is desirable in the context of iron oxide reduction via an electrochemical pathway. The addition of  $\text{Fe}^{2+}$ , either directly [7, 18, 23, 59] or in the form of  $\text{Fe}^{\text{II}}$ -containing oxides [6, 58], to achieve a targeted increase in reaction rate has been noted multiple times in the literature.

For the OxA concentration used in this study, approx. 6% of the  $\text{Fe}^{2+}$  exists in form of  $\text{Fe}^{\text{II}}\text{C}_2\text{O}_4$  in equilibrium, as shown in Fig. 8. From that figure it also becomes evident that this is the only stable  $\text{Fe}^{2+}$  complex in solution participating in the autocatalytic pathway (Eq. A.6), since all the remaining ferrous ions are uncomplexed. If the pH is adjusted independently as e.g. in the experiments conducted by Lee et al. [60], the maximum in reaction rate actually coincides with the peak of  $\text{Fe}^{\text{II}}\text{C}_2\text{O}_4$  in equilibrium for that OxA concentration (Fig. C.20 in the Appendix) and decreases for increasing pH values. This means that even if other ferrous complexes are present,  $\text{Fe}^{\text{II}}\text{C}_2\text{O}_4$  is still the dominant complex participating in the autocatalytic pathway.

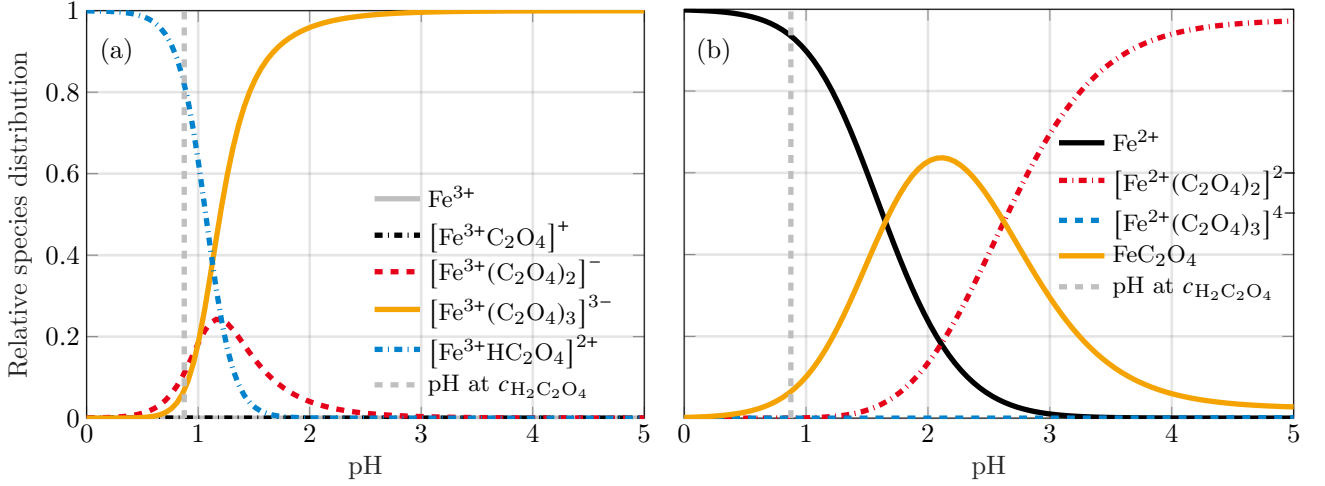


Figure 8: Relative distribution of ferric (Fig. a) and ferrous (Fig. b) species as a function of pH, calculated using the equilibrium constant values from Pnias et al. [20] and Pozdnyakov et al. [65]. Additionally, the pH at  $c_{\text{H}_2\text{C}_2\text{O}_4} = 0.45 \text{ mol/l}$  in the present study, assuming the dissociation of OxA with  $\text{pK}_{\text{a}1} = 1.25$  and  $\text{pK}_{\text{a}2} = 4.21$  at  $25^\circ\text{C}$  [19].

While the presence of  $\text{Fe}^{\text{II}}\text{C}_2\text{O}_4$  accelerates the dissolution process, it is adversely affected once the solubility limit of  $\text{Fe}^{\text{II}}\text{C}_2\text{O}_4$  is reached, leading to the precipitation of a solid product. If the oxide particles themselves act as nucleation points, a solid product layer forms around the particles and hinders further dissolution. Even in the case of homogeneous precipitation, the iron would still be lost to the solid, complicating subsequent processing steps in the context of electrowinning. As shown in Fig. 8, the fraction of ferrous oxalate in solution remains substantial at higher pH values due to the increasing proportion of doubly deprotonated oxalate ions  $\text{C}_2\text{O}_4^{2-}$ . To completely prevent the formation of ferrous oxalate, the pH could be lowered towards zero, at which point the fraction of uncomplexed ferrous iron approaches one. However, this would likely result in slower reaction rates, as  $\text{Fe}^{\text{II}}\text{C}_2\text{O}_4$  appears to be the dominant complex driving the autocatalytic mechanism. To mitigate these effects, the concentration of OxA could be increased to its solubility limit (approximately  $1 \text{ mol/l}$  at room temperature [36]). However, this does not address other potential influences, such as the dynamic nature of the process, which would render the equilibrium diagrams in Fig. 8 invalid. Furthermore, the pH naturally shifts during the reaction depending on the initial OxA concentration and pH, as the formation of oxalate-containing complexes leads to subsequent dissociation of oxalic acid (Eq. A.1), as discussed in detail by Santawaja et al. [36]. There may also be local effects, as suggested by Vehmaanperä et al. [35], where the depletion of  $\text{H}^+$  near the particle surface leads to a higher local pH compared to the bulk solution. Although it is possible to adjust the concentration of iron oxide in solution such that the maximum ferrous oxalate concentration remains below its solubility limit, this approach is inefficient from an industrial perspective. Additionally, estimating the exact concentration of ferrous iron can be challenging due to the dynamic and interconnected boundary conditions. Finally, another method to suppress the formation of humboldtine is the use of an oxalic/nitric acid mixture, as described by Vehmaanperä et al. [35]. In their experiments with an excess of iron oxide to determine solubility limits, the pH at the end of dissolution reached values as high as 0.6 for both magnetite and hematite. Thus, combining their results with the species distribution shown in Fig. 8

b), it appears that the role of nitric acid in preventing ferrous oxalate formation extends beyond merely lowering pH, as the reported pH values still fall within the stable range of  $\text{Fe}^{\text{II}}\text{C}_2\text{O}_4$ .

In the present case,  $\text{Fe}^{2+}$  can originate from multiple sources, but at the beginning of an experiment, the most significant influence likely comes from short-wavelength light. This can reduce terminal  $\text{Fe}^{\text{II}}$  in the hematite shell directly, as well as ferric complexes (see Fig. 1), which are stable at the OxA concentration used in the present study (see Eq. A.7 and Fig. 8). As the reaction progresses and the core of the particles becomes exposed to the acid,  $\text{Fe}^{\text{II}}$  within the crystal is also available, eliminating the need for  $\text{Fe}^{3+}$  or  $\text{Fe}^{\text{III}}$  reduction to form ferrous complexes. In order to form  $\text{Fe}^{\text{II}}\text{C}_2\text{O}_4$ , the doubly deprotonated oxalate ion is required (Eq. A.8). While the fraction of  $\text{C}_2\text{O}_4^{2-}$  in the solution is only around 0.01%, as estimated from equilibrium diagrams at the concentration of oxalic acid used (see e.g. [24]), it could still react directly to form  $\text{Fe}^{\text{II}}\text{C}_2\text{O}_4$ , either in solution or at the particle surface. In a previous study [37], where the reaction products were swept away from the site, the gradual reduction of magnetite was observed. However, unlike in other studies [32, 35, 66], no crystalline humboldtine formed; instead, an amorphous structure was detected. This suggests that interactions with the reaction products are crucial in the formation of ferrous oxalate precipitates. Specifically for the dissolution of CIPs, the process was observed to be non-reductive in the absence of product interaction [37]. In the present case, with self-interaction permitted, Fig. 7 suggests that the lack of crystalline precipitate formation could simply be due to the reaction not having progressed far enough. Further insights into the role of ferrous iron in the dissolution of CIPs are provided by the segmented experimental runs, which have been fitted using two linear models, as described in Sec. 3.1. The majority of segmented rates occurred at experiments at  $80^\circ\text{C}$ , however there are also two experimental runs at lower temperatures, as shown in Fig. 9.

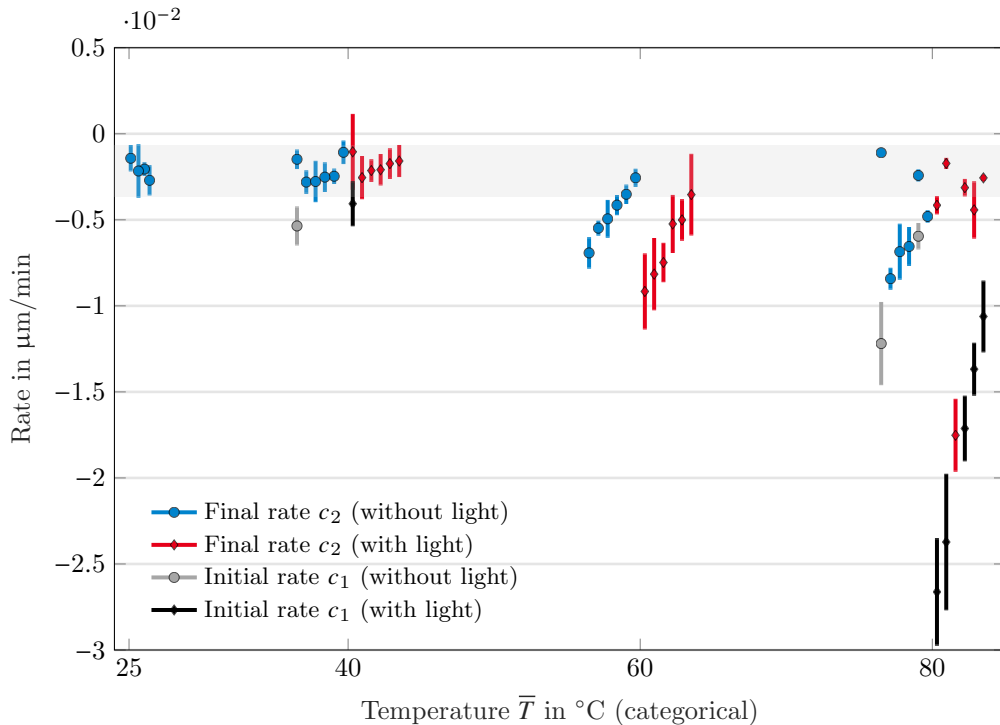


Figure 9: Estimated  $d\bar{d}/dt$  ( $c_1$  and  $c_2$ ) as a function of temperature both with and without light. For better visibility the data has been distributed and ordered according to the  $c_1$  value at each temperature level.

At the elevated temperature of  $80^\circ\text{C}$ , almost all experiments with light exposure exhibit two significantly different rates, as also evident from the unfitted data in Fig. 3. Given the complex species distribution and the internal Fe phase structure of the CIPs, it is likely that the formation of a solid product layer is responsible for the decrease in reaction rate. This could occur indirectly through precipitation from the solution or directly through the reaction with the exposed magnetite core interspersed with hematite spikes. As summarized in Sec. 1.2, current models

assume a diffusively limited growth of a hematite shell during the final stages of the combustion process [47, 51]. If, as Mi et al. [47] argue, the final hematite thickness is solely a function of the ambient oxygen concentration during combustion, this would lead to an equal hematite layer thickness across all particle sizes (neglecting curvature effects). Since the dissolution of iron oxides is surface-reaction controlled [18, 23, 25], the hematite shell would only dissolve simultaneously across particles if they were uniform in size. However, as shown by Buchheiser et al. [55], the majority of particles are approximately 8–10  $\mu\text{m}$  in diameter. Consequently, not all particles reach the core simultaneously, but the majority do at approximately the same time. Therefore, the factors responsible for the sudden decrease in reaction rate are likely interconnected, occurring once a significant portion of the particles has dissolved: either light-assisted reductive dissolution has triggered the precipitation of solid ferrous oxalate, the magnetite core has become exposed, or both processes are contributing simultaneously.

#### 4. Conclusion

This study examined the effects of temperature (40 - 80°C) and light exposure (190 to 2500 nm at 1.6 mW) on the dissolution behavior of combusted iron particles (CIPs) in oxalic acid (0.45 mol/L). The CIPs were generated at three different fuel-to-air equivalence ratios: 0.67, 1.0, and 1.5. The particles were identified through post-processing of collected images to determine their size and morphology distribution.

Optical measurements revealed that particles exist as clusters, which break apart due to interactions with the flow, with other clusters and with the walls of the reaction vessel. The combined effects of cluster breakup and dissolution resulted in an almost linear decrease in median particle diameter over time. Statistical analysis indicated that both light and temperature can increase the particle dissolution rate, with an interaction between the two parameters. Increasing temperature causes an increase in particle shrinking rate, while light irradiation enhanced the rate only at higher temperatures. This behavior is attributed to the slow light- and temperature-dependent reaction rate of the hematite shell of the CIPs, necessitating a sufficient concentration of iron in solution for an effective reduction by light and subsequent acceleration of the dissolution. Although literature suggests that increasing the fuel-to-air equivalence ratio enhances the fraction of magnetite, it does not significantly affect the dissolution rate. This is surprising, considering that magnetite increases the reaction rate both through its spinel-type crystal structure and ferrous ions which activate the autocatalytic pathway that would be expected to result in a self-reinforcing process. At elevated temperatures, particularly under light exposure, an sudden decrease in the rate of particle size reduction was observed during the dissolution process. This phenomenon may result from the homogeneous formation of solid ferrous oxalate once the solubility limit is reached, with the remaining particles serving as nucleation sites for the solid layer. Additionally, the solid product layer could form due to exposure of the magnetite core, leading to a sudden increase in available ferrous iron directly on the particle surface. These two mechanisms are not mutually exclusive and may contribute simultaneously to the observed behavior. The formation of a solid precipitate is undesirable in electrowinning processes, as it not only slows the reaction rate but results also in the conversion of iron to a product requiring further processing.

From these results, and considering the stable iron oxalate complexes, it is concluded that for the efficient dissolution of CIPs, a temperature above 60°C is recommended, along with the maximum concentration of OxA, which has a solubility limit of approximately 1 mol/L at room temperature. If independent pH adjustment is feasible, lower values are preferable to limit ferrous oxalate formation below its solubility threshold. However, completely suppressing ferrous oxalate is not advisable, as this significantly slows the dissolution process due to the necessity of ferrous iron for activating the autocatalytic mechanism that increases the dissolution rate in a self-reinforcing process. Given the structure of the CIPs, this initial activation may require short-wavelength light or the addition of ferrous salts,

as the hematite shell obstructs access to the magnetite core (which contains Fe<sup>II</sup>). A potential solution to the rapid increase in ferrous ions once the magnetite core is exposed could involve using acid mixtures, such as nitric acid [35]. These mixtures seem to prevent solid formation without impeding the autocatalytic pathway. This approach would be particularly promising as an additive in OxA-based deep eutectic solvents.

### Author contributions

**M. Lausch:** Writing – original draft (lead), Visualization (lead), Validation (lead), Software (lead), Methodology (equal), Investigation (equal), Formal analysis (lead), Conceptualization (supporting). **Y. Ruan:** Investigation (equal). **P. Brockmann:** Writing – original draft (supporting), Writing – review & editing (equal). **A. Zimina:** Writing – original draft (supporting), Writing – review & editing (equal). **B.J.M. Etzold:** Writing – review & editing (equal), Supervision, Resources, Methodology (equal), Conceptualization (equal) **J. Hussong:** Writing – review & editing (equal), Supervision, Resources, Funding acquisition (lead), Conceptualization (equal).

### Acknowledgements

This work was funded by the Hessian Ministry of Higher Education, Research, Science and the Arts - cluster project Clean Circles. Thanks to Reda Kamal for his insightful discussions. We thank the Institute of Materials Science at the Technical University Darmstadt for the access to the scanning electron microscope and J. Schmidpeter and P. Neuhäusel in particular for their help during its operation. Parts of this work have been improved grammatically and stylistically using language models, including ChatGPT (OpenAI) and DeepL Write (DeepL SE). We thank the Institute for Applied Materials (IAM) at Karlsruhe Institute of Technology (KIT) and R. Pashminehazar in particular for the X-ray computed tomography experiments.

### References

- [1] Y. Lv, J. Liu, R. Zhu, J. Zhu, Q. Chen, X. Liang, H. He, Photoreductive dissolution of iron (hydr)oxides and its geochemical significance, *ACS Earth and Space Chemistry* 6 (2022) 811–829. doi:10.1021/acsearthspacechem.1c00334.
- [2] N.-H. Yin, P. Louvat, A. Thibault-DE-Chanvalon, M. Sebiló, D. Amouroux, Iron isotopic fractionation driven by low-temperature biogeochemical processes, *Chemosphere* 316 (2023) 137802. doi:https://doi.org/10.1016/j.chemosphere.2023.137802.
- [3] K. Barbeau, E. L. Rue, K. W. Bruland, A. Butler, Photochemical cycling of iron in the surface ocean mediated by microbial iron(iii)-binding ligands, *Nature* 413 (2001) 409–413. doi:10.1038/35096545.
- [4] W. Riemenschneider, M. Tanifuji, *Oxalic Acid*, John Wiley & Sons, Ltd, 2011, p. 537. doi:https://doi.org/10.1002/14356007.a18\_247.pub2.
- [5] E. B. Borghi, S. P. Alí, P. J. Morando, M. A. Blesa, Cleaning of stainless steel surfaces and oxide dissolution by malonic and oxalic acids, *Journal of Nuclear Materials* 229 (1996) 115–123. doi:https://doi.org/10.1016/0022-3115(95)00201-4.
- [6] A. Martínez-Luévanos, M. Rodríguez-Delgado, A. Uribe-Salas, F. Carrillo-Pedroza, J. Osuna-Alarcón, Leaching kinetics of iron from low grade kaolin by oxalic acid solutions, *Applied Clay Science* 51 (2011) 473–477. doi:https://doi.org/10.1016/j.clay.2011.01.011.

- [7] V. Ambikadevi, M. Lalithambika, Effect of organic acids on ferric iron removal from iron-stained kaolinite, *Applied Clay Science* 16 (2000) 133–145. doi:[https://doi.org/10.1016/S0169-1317\(99\)00038-1](https://doi.org/10.1016/S0169-1317(99)00038-1).
- [8] IEA, Iron and Steel, Technical Report, International Energy Agency, 2022. URL: <https://www.iea.org/reports/iron-and-steel>.
- [9] K. Meijer, C. Zeilstra, C. Teerhuis, M. Ouwehand, J. van der Stel, Developments in Alternative Ironmaking, *Transactions of the Indian Institute of Metals* 66 (2013) 475–481. doi:10.1007/s12666-013-0309-z.
- [10] A. Hasanbeigi, M. Arens, L. Price, Alternative emerging ironmaking technologies for energy-efficiency and carbon dioxide emissions reduction: A technical review, *Renewable and Sustainable Energy Reviews* 33 (2014) 645–658. doi:<https://doi.org/10.1016/j.rser.2014.02.031>.
- [11] L. D. Harvey, Iron and steel recycling: Review, conceptual model, irreducible mining requirements, and energy implications, *Renewable and Sustainable Energy Reviews* 138 (2021) 110553. doi:<https://doi.org/10.1016/j.rser.2020.110553>.
- [12] Worldsteel Association, World Steel in Figures 2024, Technical Report, Worldsteel Association, 2024. <https://worldsteel.org/data/world-steel-in-figures-2024/>, Last accessed on 2024-10-24.
- [13] P. Debiagi, R. Rocha, A. Scholtissek, J. Janicka, C. Hasse, Iron as a sustainable chemical carrier of renewable energy: Analysis of opportunities and challenges for retrofitting coal-fired power plants, *Renewable and Sustainable Energy Reviews* 165 (2022) 112579. doi:<https://doi.org/10.1016/j.rser.2022.112579>.
- [14] J. Bergthorson, S. Goroshin, M. Soo, P. Julien, J. Palecka, D. Frost, D. Jarvis, Direct combustion of recyclable metal fuels for zero-carbon heat and power, *Applied Energy* 160 (2015) 368–382. doi:<https://doi.org/10.1016/j.apenergy.2015.09.037>.
- [15] J. M. Bergthorson, Recyclable metal fuels for clean and compact zero-carbon power, *Progress in Energy and Combustion Science* 68 (2018) 169–196. doi:<https://doi.org/10.1016/j.pecs.2018.05.001>.
- [16] P. Tóth, Y. Ögren, A. Sepman, P. Gren, H. Wiinikka, Combustion behavior of pulverized sponge iron as a recyclable electrofuel, *Powder Technology* 373 (2020) 210–219. doi:<https://doi.org/10.1016/j.powtec.2020.05.078>.
- [17] L. Dirven, N. G. Deen, M. Golombok, Dense energy carrier assessment of four combustible metal powders, *Sustainable Energy Technologies and Assessments* 30 (2018) 52–58. doi:<https://doi.org/10.1016/j.seta.2018.09.003>.
- [18] M. I. Litter, M. A. Blesa, Photodissolution of iron oxides. iv. a comparative study on the photodissolution of hematite, magnetite, and maghemite in edta media, *Canadian Journal of Chemistry* 70 (1992) 2502–2510. doi:10.1139/v92-316.
- [19] D. Papias, M. Taxiarchou, I. Paspaliaris, A. Kontopoulos, Mechanisms of dissolution of iron oxides in aqueous oxalic acid solutions, *Hydrometallurgy* 42 (1996) 257–265. doi:[https://doi.org/10.1016/0304-386X\(95\)00104-0](https://doi.org/10.1016/0304-386X(95)00104-0).
- [20] D. Papias, M. Taxiarchou, I. Douni, I. Paspaliaris, A. Kontopoulos, Thermodynamic analysis of the reactions of iron oxides: Dissolution in oxalic acid, *Canadian Metallurgical Quarterly* 35 (1996) 363–373. doi:[https://doi.org/10.1016/S0008-4433\(96\)00018-3](https://doi.org/10.1016/S0008-4433(96)00018-3).

- [21] W. Stumm, Aquatic surface chemistry: Chemical processes at the particle-water interface, volume 87, John Wiley & Sons, 1987.
- [22] R. M. Sellers, W. J. Williams, High-temperature dissolution of nickel chromium ferrites by oxalic acid and nitrilotriacetic acid, *Faraday Discuss. Chem. Soc.* 77 (1984) 265–274. doi:10.1039/DC9847700265.
- [23] M. A. Blesa, H. A. Marinovich, E. C. Baumgartner, A. J. G. Maroto, Mechanism of dissolution of magnetite by oxalic acid-ferrous ion solutions, *Inorganic Chemistry* 26 (1987) 3713–3717. doi:10.1021/ic00269a019.
- [24] M. Lausch, P. Brockmann, F. Schmitt, B. Etzold, J. Hussong, In-situ iron oxide particle size and shape evolution during the dissolution in oxalic acid, *Chemical Engineering Science* (2024) 119864. doi:https://doi.org/10.1016/j.ces.2024.119864.
- [25] M. I. Litter, E. C. Baumgartner, G. A. Urrutia, M. A. Blesa, Photodissolution of iron oxides. 3. interplay of photochemical and thermal processes in maghemite/carboxylic acid systems, *Environmental science & technology* 25 (1991) 1907–1913.
- [26] W. Stumm, B. Sulzberger, The cycling of iron in natural environments: Considerations based on laboratory studies of heterogeneous redox processes, *Geochimica et Cosmochimica Acta* 56 (1992) 3233–3257. doi:https://doi.org/10.1016/0016-7037(92)90301-X.
- [27] T. Hiemstra, W. H. Van Riemsdijk, Effect of different crystal faces on experimental interaction force and aggregation of hematite, *Langmuir* 15 (1999) 8045–8051. doi:10.1021/1a9903604.
- [28] P. Joshi, C. A. Gorski, Anisotropic morphological changes in goethite during  $Fe^{2+}$ -catalyzed recrystallization, *Environmental Science & Technology* 50 (2016) 7315–7324. doi:10.1021/acs.est.6b00702.
- [29] S. V. Yanina, K. M. Rosso, Linked Reactivity at Mineral-Water Interfaces Through Bulk Crystal Conduction, *Science* 320 (2008) 218–222. doi:10.1126/science.1154833.
- [30] J. S. Colton, S. D. Erickson, T. J. Smith, R. K. Watt, Sensitive detection of surface- and size-dependent direct and indirect band gap transitions in ferritin, *Nanotechnology* 25 (2014) 135703. doi:10.1088/0957-4484/25/13/135703.
- [31] T. R. Hogness, W. C. Johnson, Qualitative analysis and chemical equilibrium, revised edition, Henry Holt and Company, New York, 1940.
- [32] P. Santawaja, S. Kudo, A. Mori, A. Tahara, S. Asano, J.-i. Hayashi, Sustainable iron-making using oxalic acid: The concept, a brief review of key reactions, and an experimental demonstration of the iron-making process, *ACS Sustainable Chemistry & Engineering* 8 (2020) 13292–13301. doi:10.1021/acssuschemeng.0c03593.
- [33] D. M. Sherman, Electronic structures of iron(III) and manganese(IV) (hydr)oxide minerals: Thermodynamics of photochemical reductive dissolution in aquatic environments, *Geochimica et Cosmochimica Acta* 69 (2005) 3249–3255. doi:https://doi.org/10.1016/j.gca.2005.01.023.
- [34] E. Baumgartner, M. Blesa, H. Marinovich, A. Maroto, Heterogeneous electron transfer as a pathway in the dissolution of magnetite in oxalic acid solutions, *Inorganic Chemistry* 22 (1983) 2224–2226. doi:10.1021/ic00158a002.
- [35] P. Vehmaanperä, T. Sihvonen, R. Salmimies, A. Häkkinen, Dissolution of magnetite and hematite in mixtures of oxalic and nitric acid: Mechanisms and kinetics, *Minerals* 12 (2022). doi:10.3390/min12050560.

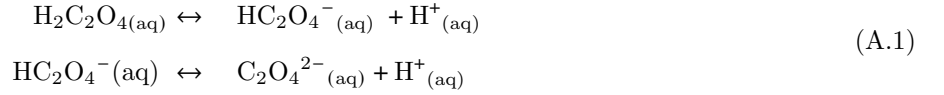
- [36] P. Santawaja, S. Kudo, A. Tahara, S. Asano, J. ichiro Hayashi, Dissolution of iron oxides highly loaded in oxalic acid aqueous solution for a potential application in iron-making, *ISIJ International* advpub (2021) ISIJINT-2020-726. doi:10.2355/isijinternational.ISIJINT-2020-726.
- [37] M. Lausch, A. Zimina, J. Bao, R. Pashminehazar, B. J. M. Etzold, U. I. Kramm, J.-D. Grunwaldt, J. Hussong, New insights into the dissolution mechanisms of iron oxides and combusted iron particles in oxalic acid, *The Journal of Chemical Physics* 161 (2024) 194308. URL: <https://doi.org/10.1063/5.0229410>. doi:10.1063/5.0229410.
- [38] J. Kabai, Determination of specific activation energies of metal oxides and metal hydrates by measurement of the rate of dissolution, *Acta Chimica Academiae Scientiarum Hungaricae* 78 (1973) 57–73.
- [39] H. Wiinikka, T. Vikström, J. Wennebro, P. Toth, A. Sepman, Pulverized sponge iron, a zero-carbon and clean substitute for fossil coal in energy applications, *Energy & Fuels* 32 (2018) 9982–9989. doi:10.1021/acs.energyfuels.8b02270.
- [40] P. Tóth, Y. Ögren, A. Sepman, P. Gren, H. Wiinikka, Combustion behavior of pulverized sponge iron as a recyclable electrofuel, *Powder Technology* 373 (2020) 210–219. doi:<https://doi.org/10.1016/j.powtec.2020.05.078>.
- [41] S. Li, D. Sanned, J. Huang, E. Berrocal, W. Cai, M. Aldén, M. Richter, Z. Li, Stereoscopic high-speed imaging of iron microexplosions and nanoparticle-release, *Opt. Express* 29 (2021) 34465–34476. doi:10.1364/OE.434836.
- [42] L. Choisez, N. E. van Rooij, C. J. Hessels, A. K. da Silva, I. R. S. Filho, Y. Ma, P. de Goey, H. Springer, D. Raabe, Phase transformations and microstructure evolution during combustion of iron powder, *Acta Materialia* 239 (2022) 118261. doi:<https://doi.org/10.1016/j.actamat.2022.118261>.
- [43] N. Poletaev, M. Khlebnikova, Combustion of iron particles suspension in laminar premixed and diffusion flames, *Combustion Science and Technology* 194 (2022) 1356–1377. doi:10.1080/00102202.2020.1812588.
- [44] A. Attili, P. Farmand, C. Schumann, S. Farazi, B. Böhm, T. Li, C. Geschwindner, J. Köser, A. Dreizler, H. Pitsch, Numerical Simulations and Experiments of Ignition of Solid Particles in a Laminar Burner: Effects of Slip Velocity and Particle Swelling, *Flow, Turbulence and Combustion* 106 (2021) 515–531. doi:10.1007/s10494-020-00222-1.
- [45] D. Ning, Y. Shoshin, M. van Stiphout, J. van Oijen, G. Finotello, P. de Goey, Temperature and phase transitions of laser-ignited single iron particle, *Combustion and Flame* 236 (2022) 111801. doi:<https://doi.org/10.1016/j.combustflame.2021.111801>.
- [46] S. Li, J. Huang, W. Weng, Y. Qian, X. Lu, M. Aldén, Z. Li, Ignition and combustion behavior of single micron-sized iron particle in hot gas flow, *Combustion and Flame* 241 (2022) 112099. doi:<https://doi.org/10.1016/j.combustflame.2022.112099>.
- [47] X. Mi, A. Fujinawa, J. M. Bergthorson, A quantitative analysis of the ignition characteristics of fine iron particles, *Combustion and Flame* 240 (2022) 112011. doi:<https://doi.org/10.1016/j.combustflame.2022.112011>.
- [48] F.-D. Tang, S. Goroshin, A. J. Higgins, Modes of particle combustion in iron dust flames, *Proceedings of the Combustion Institute* 33 (2011) 1975–1982. doi:<https://doi.org/10.1016/j.proci.2010.06.088>.

- [49] R. D. Jin-Hua Sun, T. Hirano, Combustion behavior of iron particles suspended in air, *Combustion Science and Technology* 150 (2000) 99–114. doi:[10.1080/00102200008952119](https://doi.org/10.1080/00102200008952119).
- [50] M. Soo, X. Mi, S. Goroshin, A. J. Higgins, J. M. Bergthorson, Combustion of particles, agglomerates, and suspensions – a basic thermophysical analysis, *Combustion and Flame* 192 (2018) 384–400. doi:<https://doi.org/10.1016/j.combustflame.2018.01.032>.
- [51] D. Ning, Y. Shoshin, J. van Oijen, G. Finotello, L. de Goey, Burn time and combustion regime of laser-ignited single iron particle, *Combustion and Flame* 230 (2021) 111424. doi:<https://doi.org/10.1016/j.combustflame.2021.111424>.
- [52] M. Soos, H. Wu, M. Morbidelli, Taylor-couette unit with a lobed inner cylinder cross section, *AIChE Journal* 53 (2007) 1109–1120. doi:<https://doi.org/10.1002/aic.11153>.
- [53] L. S. Nelson, D. E. Rosner, S. C. Kurzius, H. S. Levine, Combustion of zirconium droplets in oxygen/rare gas mixtures—kinetics and mechanism, *Symposium (International) on Combustion* 12 (1969) 59–70. doi:[https://doi.org/10.1016/S0082-0784\(69\)80392-9](https://doi.org/10.1016/S0082-0784(69)80392-9).
- [54] M. Fedoryk, B. Stelzner, S. Harth, D. Trimis, Experimental investigation of the laminar burning velocity of iron-air flames in a tube burner, *Applications in Energy and Combustion Science* 13 (2023) 100111. doi:<https://doi.org/10.1016/j.jaecs.2022.100111>.
- [55] S. Buchheiser, M. P. Deutschmann, F. Rhein, A. Allmang, M. Fedoryk, B. Stelzner, S. Harth, D. Trimis, H. Nirschl, Particle and phase analysis of combusted iron particles for energy storage and release, *Materials* 16 (2023). doi:[10.3390/ma16052009](https://doi.org/10.3390/ma16052009).
- [56] T. Li, F. Heck, F. Reinauer, B. Böhm, A. Dreizler, Visualizing particle melting and nanoparticle formation during single iron particle oxidation with multi-parameter optical diagnostics, *Combustion and Flame* 245 (2022) 112357. doi:<https://doi.org/10.1016/j.combustflame.2022.112357>.
- [57] M. P. Deutschmann, A. Sperling, E. Covini, B. Böhm, A. Dreizler, H. Nirschl, Single iron particle combustion - a morphology study of partially oxidized iron particles, *Powder Technology* 445 (2024) 120102. doi:<https://doi.org/10.1016/j.powtec.2024.120102>.
- [58] S. O. Lee, T. Tran, Y. Y. Park, S. J. Kim, M. J. Kim, Study on the kinetics of iron oxide leaching by oxalic acid, *International Journal of Mineral Processing* 80 (2006) 144–152. doi:[10.1016/j.minpro.2006.03.012](https://doi.org/10.1016/j.minpro.2006.03.012).
- [59] M. Taxiarchou, D. Panias, I. Douni, I. Paspaliaris, A. Kontopoulos, Removal of iron from silica sand by leaching with oxalic acid, *Hydrometallurgy* 46 (1997) 215–227. doi:[https://doi.org/10.1016/S0304-386X\(97\)00015-7](https://doi.org/10.1016/S0304-386X(97)00015-7).
- [60] S. O. Lee, T. Tran, B. H. Jung, S. J. Kim, M. J. Kim, Dissolution of iron oxide using oxalic acid, *Hydrometallurgy* 87 (2007) 91–99. doi:<https://doi.org/10.1016/j.hydromet.2007.02.005>.
- [61] D. M. Erceg-Hurn, V. M. Mirosevich, Modern robust statistical methods: an easy way to maximize the accuracy and power of your research., *American Psychologist* 63 (2008) 591.
- [62] P. J. Huber, Robust Estimation of a Location Parameter, *The Annals of Mathematical Statistics* 35 (1964) 73 – 101. doi:[10.1214/aoms/1177703732](https://doi.org/10.1214/aoms/1177703732).

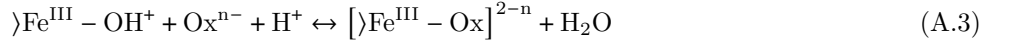
- [63] A. Dean, D. Draguljić, D. Voss, Design and Analysis of Experiments, Springer Texts in Statistics, 2nd ed. 2017 ed., Springer International Publishing : Imprint: Springer, Cham, 2017. doi:10.1007/978-3-319-52250-0.
- [64] M. Lausch, L. Reitter, M. Schremb, J. Hussong, Impact of an ice particle onto a rigid substrate: Statistical analysis of the fragment size distribution, International Journal of Impact Engineering 181 (2023) 104732. doi:<https://doi.org/10.1016/j.ijimpeng.2023.104732>.
- [65] I. P. Pozdnyakov, O. V. Kel, V. F. Plyusnin, V. P. Grivin, N. M. Bazhin, New insight into photochemistry of ferrioxalate, The Journal of Physical Chemistry A 112 (2008) 8316–8322. doi:10.1021/jp8040583, PMID: 18707071.
- [66] P. Vehmaanperä, R. Salmimies, A. Häkkinen, Thermodynamic and kinetic studies of dissolution of hematite in mixtures of oxalic and sulfuric acid, Mining Metallurgy & Exploration 38 (2020). doi:10.1007/s42461-020-00308-4.
- [67] C. Siffert, B. Sulzberger, Light-induced dissolution of hematite in the presence of oxalate. a case study, Langmuir 7 (1991) 1627–1634.
- [68] R. Cornell, P. Schindler, Photochemical dissolution of goethite in acid/oxalate solution, Clays and Clay Minerals 35 (1987) 347–352.
- [69] M. Taxiarchou, D. Pantias, I. Douni, I. Paspaliaris, A. Kontopoulos, Dissolution of hematite in acidic oxalate solutions, Hydrometallurgy 44 (1997) 287–299. doi:[https://doi.org/10.1016/S0304-386X\(96\)00075-8](https://doi.org/10.1016/S0304-386X(96)00075-8).
- [70] E. Schmider, M. Ziegler, E. Danay, L. Beyer, M. Bühner, Is it really robust?, Methodology 6 (2010) 147–151. doi:10.1027/1614-2241/a000016.
- [71] P. Ito, 7 robustness of anova and manova test procedures, in: Analysis of Variance, volume 1 of *Handbook of Statistics*, Elsevier, 1980, pp. 199–236. doi:[https://doi.org/10.1016/S0169-7161\(80\)01009-7](https://doi.org/10.1016/S0169-7161(80)01009-7).
- [72] Y. J. Kim, R. A. Cribbie, Anova and the variance homogeneity assumption: Exploring a better gatekeeper, British Journal of Mathematical and Statistical Psychology 71 (2018) 1–12. doi:<https://doi.org/10.1111/bmsp.12103>.
- [73] G. E. Box, J. S. Hunter, W. G. Hunter, et al., Statistics for experimenters, Wiley Hoboken, NJ, 2005.
- [74] R. D. Cook, S. Weisberg, Applied regression including computing and graphics, John Wiley & Sons, 2009.
- [75] I.-K. Yeo, R. A. Johnson, A new family of power transformations to improve normality or symmetry, Biometrika 87 (2000) 954–959. URL: <http://www.jstor.org/stable/2673623>.
- [76] G. E. Box, D. R. Cox, An analysis of transformations, Journal of the Royal Statistical Society Series B: Statistical Methodology 26 (1964) 211–243.
- [77] A. C. Atkinson, M. Riani, A. Corbellini, The Box–Cox Transformation: Review and Extensions, Statistical Science 36 (2021) 239 – 255. doi:10.1214/20-STS778.
- [78] M. Riani, D. Perrotta, F. Torti, FSDA: A matlab toolbox for robust analysis and interactive data exploration, Chemometrics and Intelligent Laboratory Systems 116 (2012) 17–32. doi:<https://doi.org/10.1016/j.chemolab.2012.03.017>.

## Appendix A. Occurring reaction mechanisms

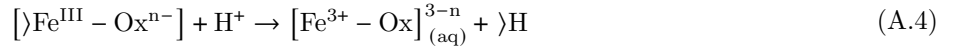
The diprotic OxA dissociates in two steps, as summarized in Eq. A.1:



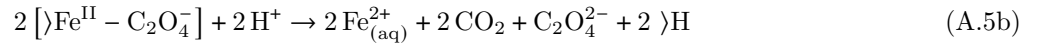
The first step in the dissolution process involves the protonation of a surface Lewis base oxide, resulting in a positively charged surface. This protonated surface then serves as the starting point for the formation of a complex with an oxalate ion from the solution (see Eq. A.3) [18, 19].



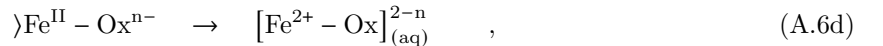
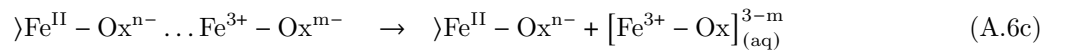
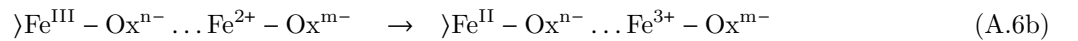
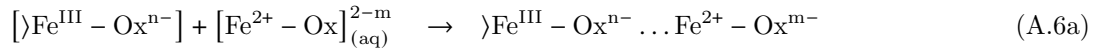
An additional non-reductive dissolution pathway involves the iron oxalate surface complex, which reacts with an additional proton to desorb into the solution, as denoted in Eq. A.4 [18, 19]



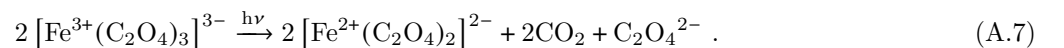
If the doubly deprotonated oxalate forms the surface complex at low concentrations of OxA, Paniais et al. [19] formulate the subsequent dissolution process based on the findings of Sellers and Williams [22] for nickel chromium ferrites, as presented in Eq. A.5b.



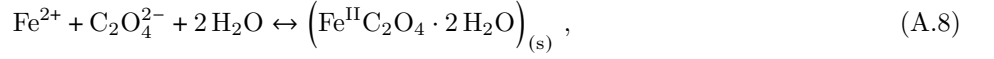
For the autocatalytic reaction, the aqueous oxalate complex transfers an electron to the  $\text{Fe}^{\text{III}}$  at the surface. The reduced surface complex subsequently detaches from the surface [18, 19]:



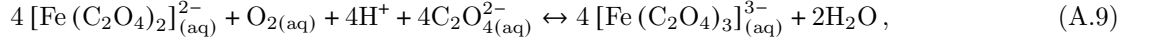
Light-driven homogeneous photolysis of the  $\text{Fe}^{3+}$  complex in solution [23, 67, 68] is described in Eq. A.7 [65]:



The systems pH controls the formation of a solid precipitate, iron(II) oxalate dihydrate [35] once its concentration has surpassed its solubility limit at  $c_{\text{FeC}_2\text{O}_4} \approx 447.2 \mu\text{mol/l}$  [31, p.487]:



Depending on the presence of dissolved oxygen in the solution, the ferrous ions in solution can be re-oxidized [69]:



## Appendix B. Statistical analysis

As stated in Sec. 3.1, the ANOVA requires mutual independence, normal distribution and equal variances of the error variable for any inference drawn to be valid. Test for mutual independence is performed by plotting standardized residuals versus run order, normal distribution by creating a normal probability plot and equal variances by inspecting standardized residuals versus their absolute fitted value of the ANOVA. As can be inferred from Fig. 7, the variance value increases with increasing temperature and is additionally a function of light irradiation (heteroscedasticity). This is also confirmed by significant fanning of the non-normally distributed standardized residuals (see Fig. B.11, B.12). This invalidates the inferences drawn from the ANOVA results [61], although the robustness of the ANOVA against violation of the prerequisites is debated [70, 71] and alternative criteria for the requirements are explored [72]. To account for both non-normality and heteroscedasticity, a data transformation is performed. There are numerous ways for data transformation (see e.g. [73, pp. 317-329], [74, pp. 316-331] and [75]) with the general goal of variance stabilization and restoring normal distribution. Since the data does not include  $|c_1| = 0$ , the widely used Box-Cox transformation technique [76] is feasible. The transformation is defined as [76, 77]

$$\Xi = \begin{cases} (|c_1|^\zeta - 1) / \zeta & \zeta \neq 0 \\ \ln(|c_1|) & \zeta = 0, \end{cases} \quad (\text{B.1})$$

where the optimal exponent  $\zeta = -0.048$  is the maximum-likelihood estimate of the profile-log-likelihood using a MATLAB-based statistics software [78]. Note that due to the requirement of strictly positive data the absolute value of  $c_1$  is used. Since all  $c_1$  values are smaller than zero and none of the values is exactly zero this does not influence the validity of the interpretation. After inspection of the standardized residuals, the ANOVA is again computed using  $\Xi$ .

To investigate the direction and magnitude of change, the values of  $\Xi$  are shown as a function of the significant terms in Fig. B.10. The errorbars indicate the transformed uncertainties of  $c_1$  using Eq. B.1. Note that for the computation of the ANOVA, the values of the factor levels of the rates are decisive, indicated by their respective marker. Focusing first on Fig. B.10(a), increasing temperature generally results in an increasing rate, which is further elevated with the supply of light irradiation. The influence of light is visible mainly at  $\bar{T} = 80^\circ\text{C}$  both in Fig. B.10(a) and (b). An increase in reaction due to the presence of light is expected, given its influence on some of the mechanisms (Fig. 1).

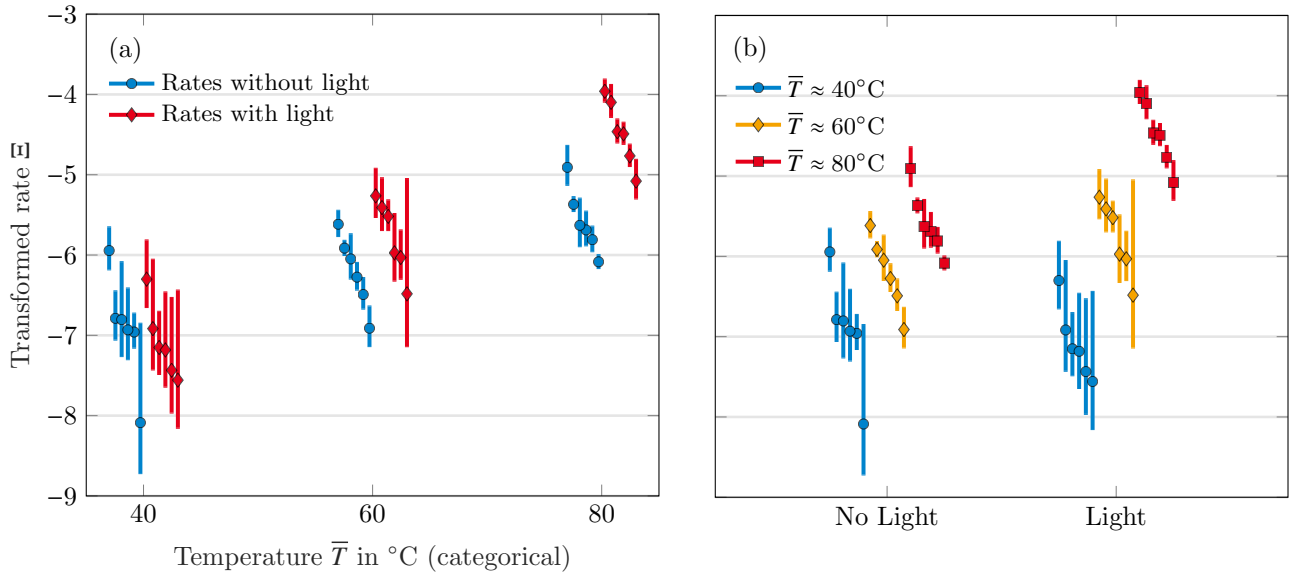


Figure B.10: (a) Effect of temperature on the transformed rate  $\Xi$ . For better visibility the data has been distributed and ordered according to the value of  $\Xi$  at each temperature level. The true, measured values of  $\bar{T}$  are shown e.g. in Fig. 7. The effect of light at a given temperature level can be inferred from the color coding. (b) Effect of light on the transformed rate  $\Xi$ , color-coded for each temperature level.

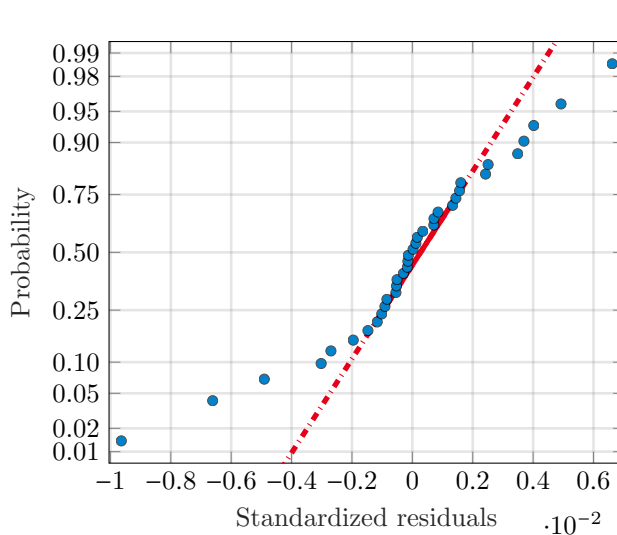


Figure B.11: Normal probability plot of untransformed  $c_1$  data.

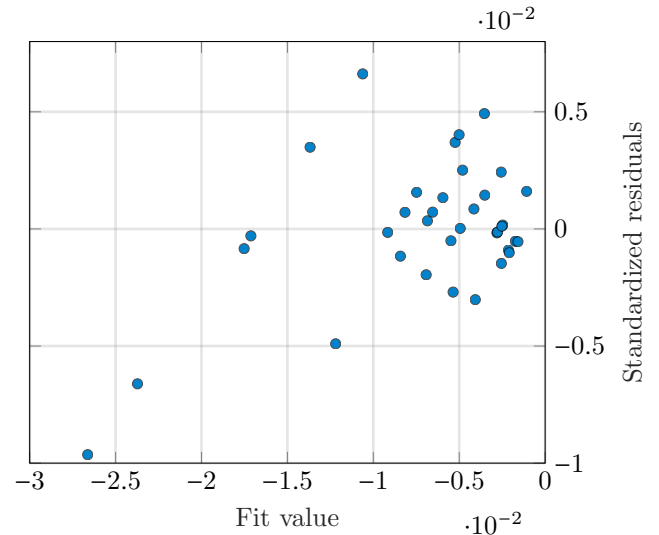


Figure B.12: Heteroscedasticity of untransformed  $c_1$  data (ANOVA).

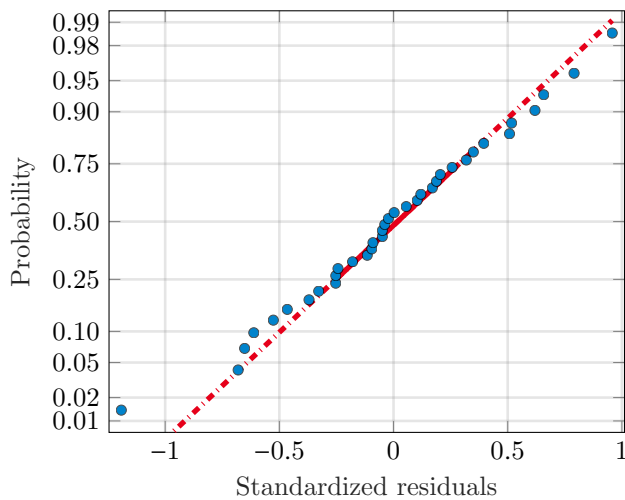


Figure B.13: Normal probability plot of  $\Xi$  data.

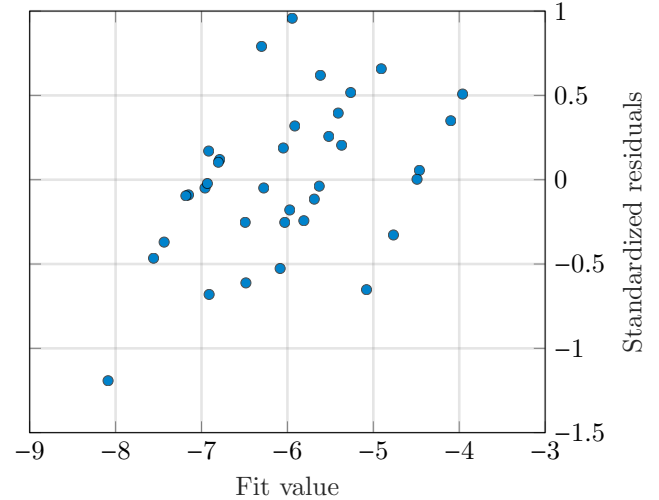


Figure B.14: Homoscedasticity of  $\Xi$  data (ANOVA).

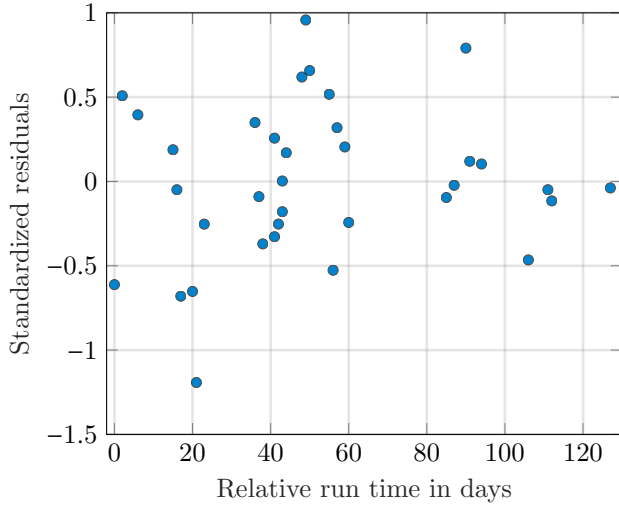


Figure B.15: Mutual independence plot of  $\Xi$  data (ANOVA).

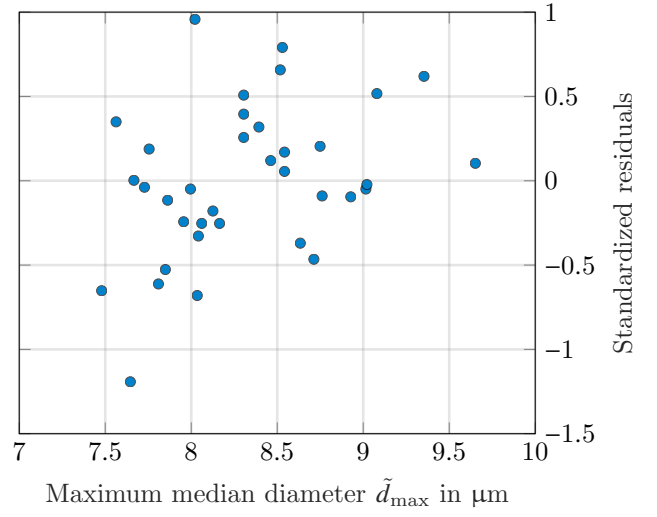


Figure B.16: Correlation plot of maximum diameter  $\tilde{d}_{\max}$ .

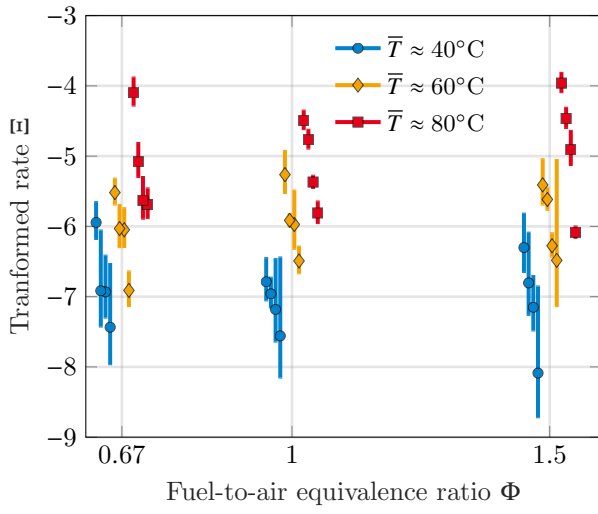


Figure B.17: Effect of  $\Phi$  on the transformed rate  $\Xi$ .

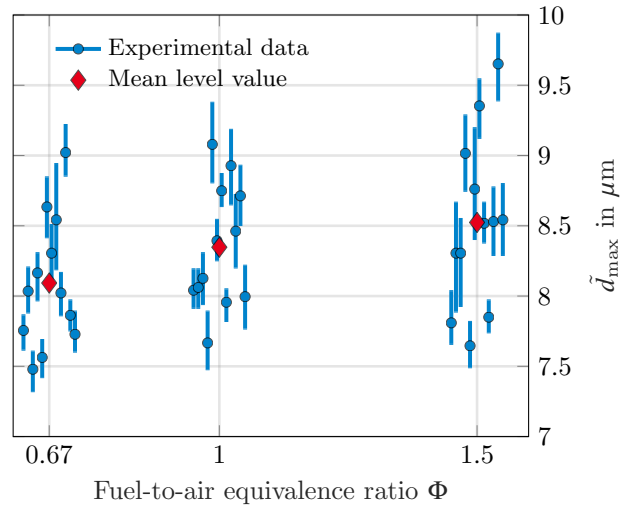


Figure B.18: Maximum median particle diameter  $\tilde{d}_{\max}$  as a function of  $\Phi$ . The error bars indicate the  $\tilde{d}_{95, \text{boot}}$  at  $t(\tilde{d} = \tilde{d}_{\max})$ .

## Appendix C. Speciation of iron oxalate complexes

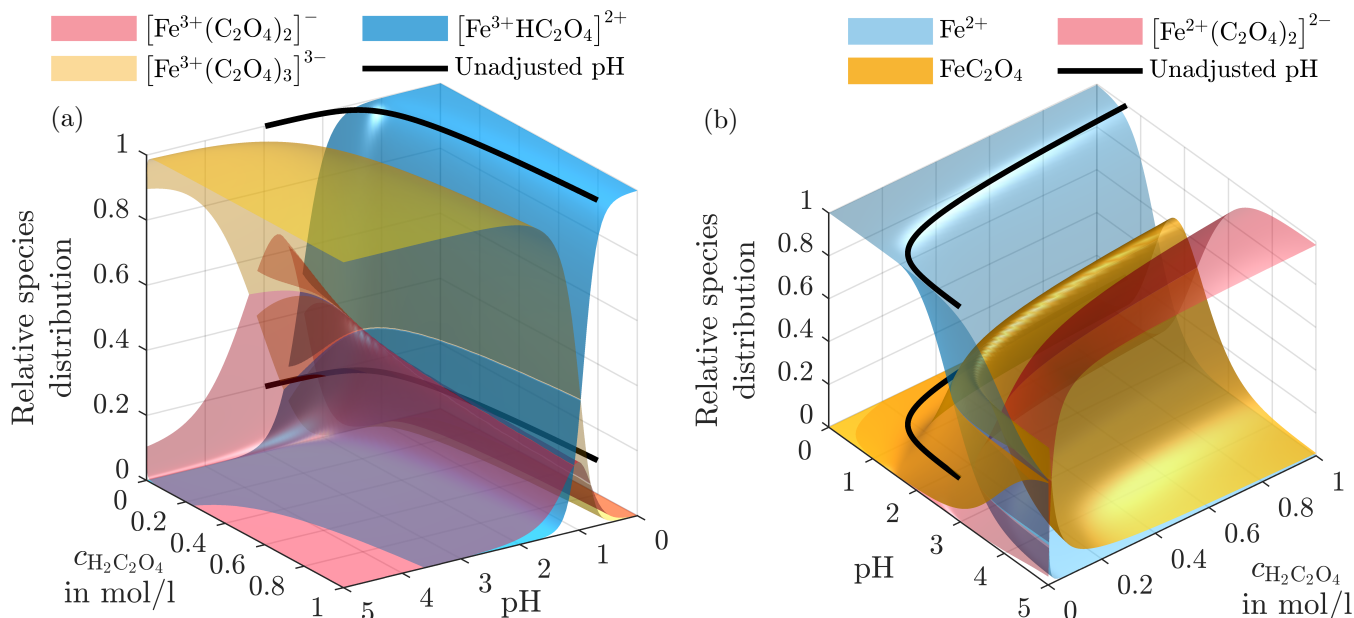


Figure C.19: Relative species distribution of ferric (a) and ferrous (b) complexes as a function of pH and  $c_{\text{H}_2\text{C}_2\text{O}_4}$ . In Fig. a) uncomplexed  $\text{Fe}^{3+}$  have been omitted due to their negligible contribution. The black lines represent the unadjusted pH at that concentration of  $\text{Ox}A$ .

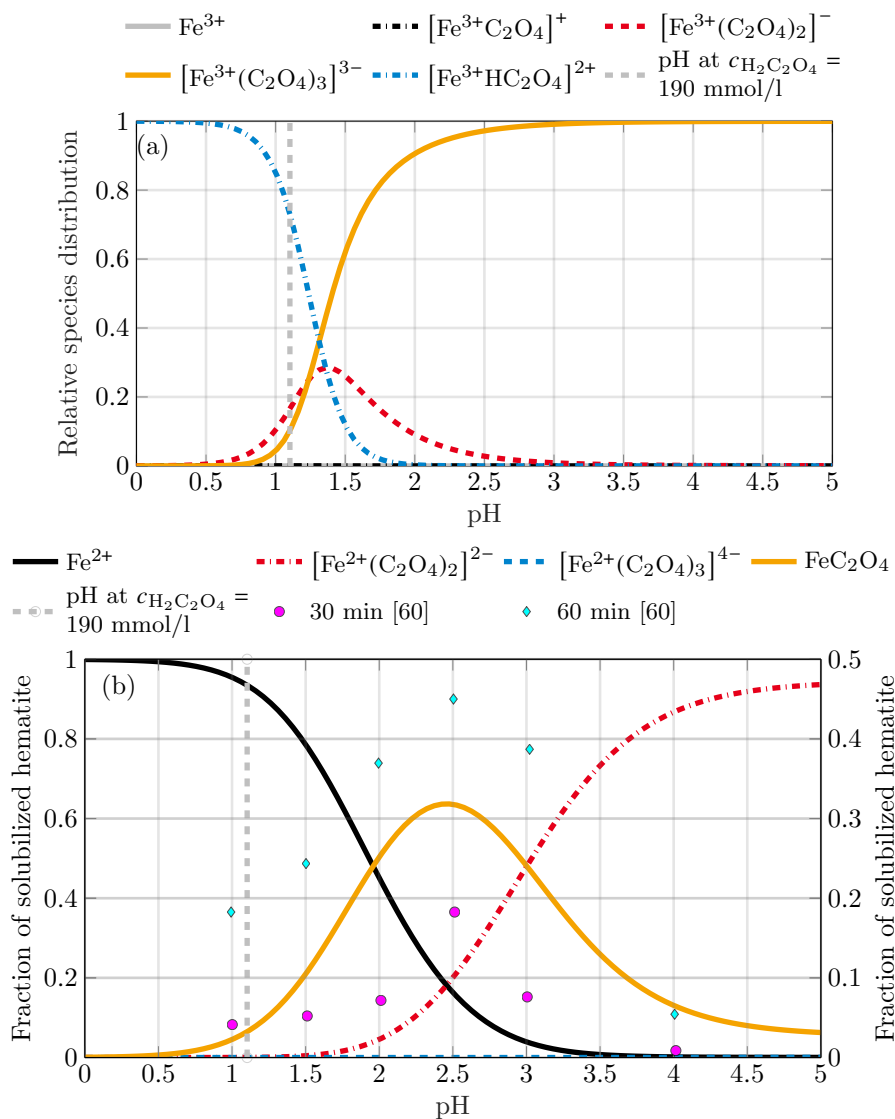


Figure C.20: Relative distribution of ferric (Fig. a) and ferrous (Fig. b) species as a function of pH, calculated using the equilibrium constant values from Panias et al. [20] and Pozdnyakov et al. [65]. The pH at  $c_{\text{H}_2\text{C}_2\text{O}_4} = 0.19$  mol/l is calculated assuming the dissociation constants  $\text{p}K_{a1} = 1.25$  and  $\text{p}K_{a2} = 4.21$  at  $25^\circ\text{C}$  [19]. The data points represent the measured fraction of total dissolved iron as a function of pH at  $c_{\text{H}_2\text{C}_2\text{O}_4} = 0.19$  mol/l, obtained from Lee et al. [60]. Reproduced with permission from Elsevier.

## Appendix D. Supplementary experimental data

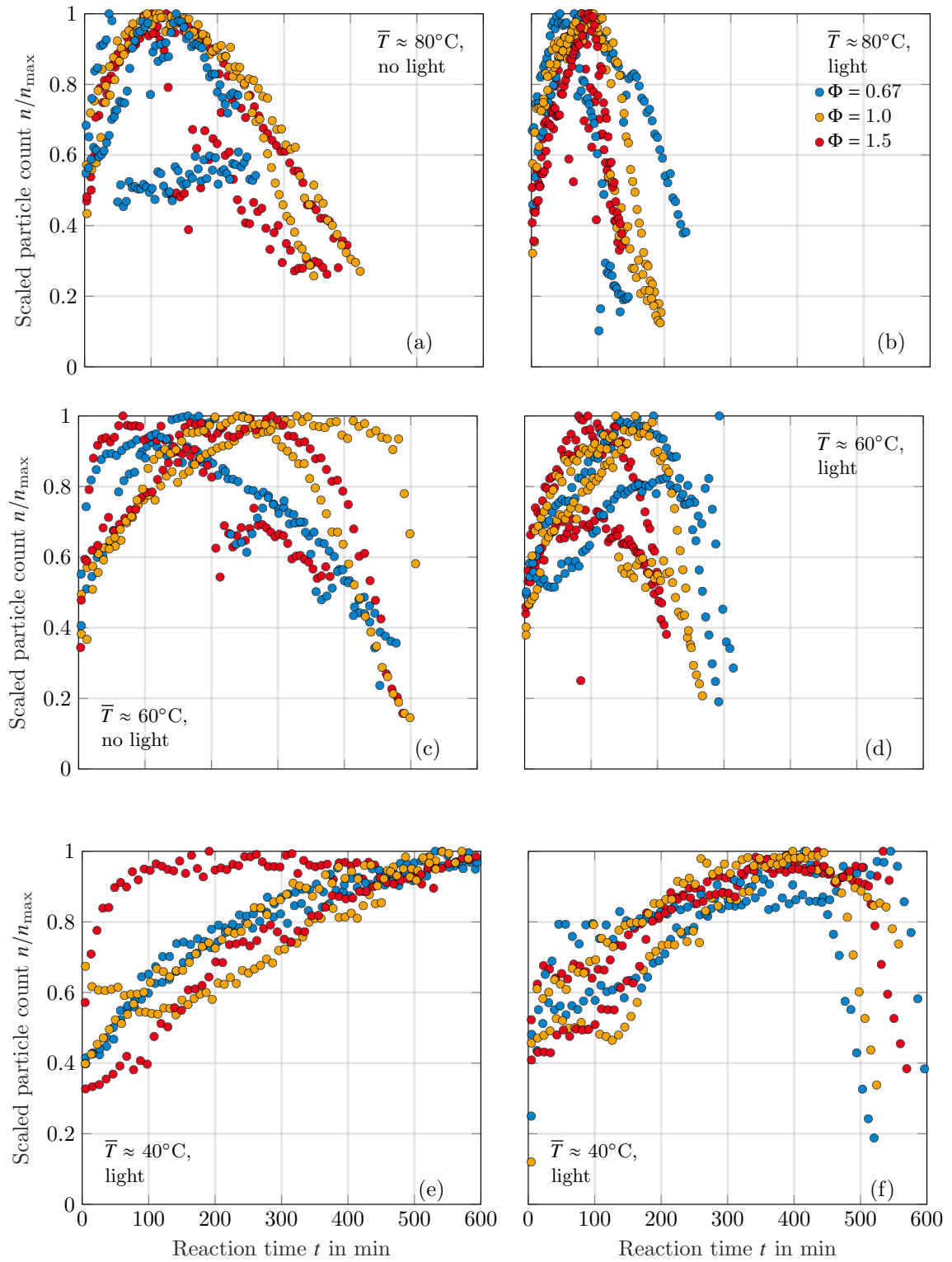


Figure D.21: Number of detected particles  $n(t)/n_{\max}$  at  $\bar{T} = 80^\circ\text{C}$  (a,b),  $60^\circ\text{C}$  (c,d) and  $40^\circ\text{C}$  (e,f), both with (a,c,e) and without (b,d,f) light irradiation for varying  $\Phi$  (0.67, 1.0, 1.5), each measured two times.

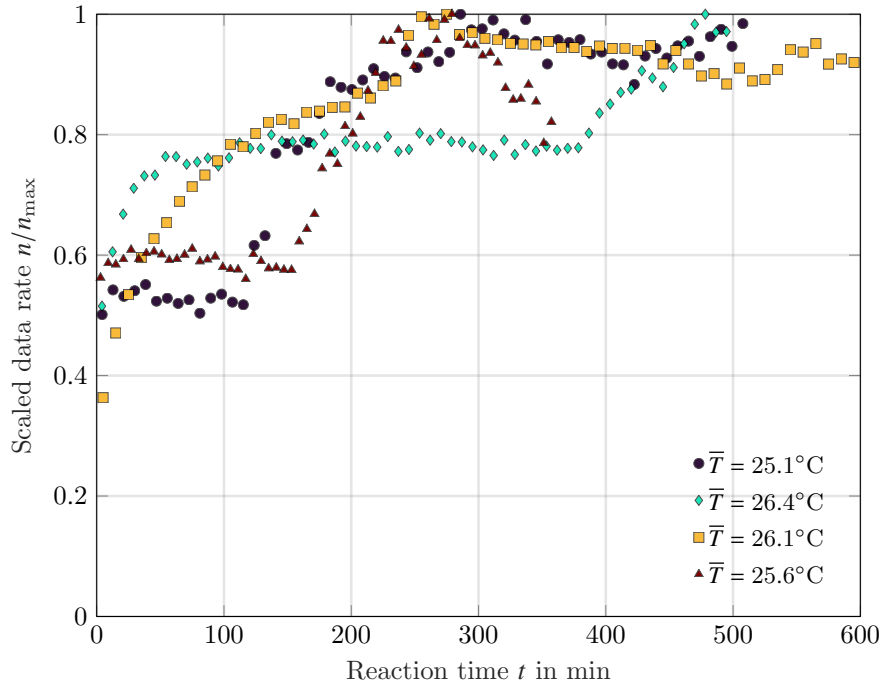


Figure D.22: Median particle diameter  $\tilde{d}(t)$  at room temperature without light irradiation for  $\Phi = 0.67$ .

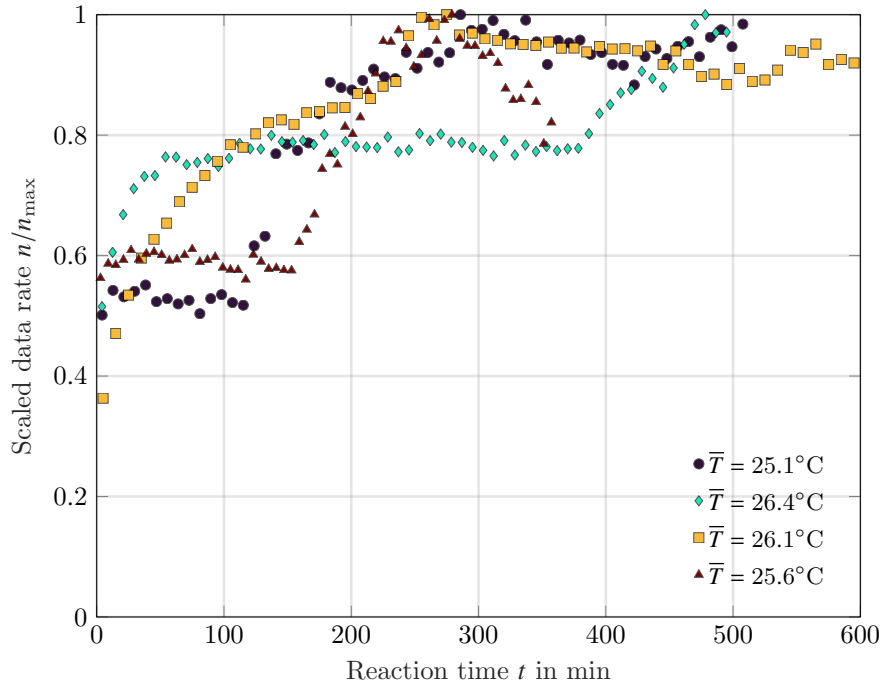


Figure D.23: Number of detected particles  $\tilde{n}(t)/n_{\max}$  at room temperature without light irradiation for  $\Phi = 0.67$ .

## Appendix E. Microtomography data evaluation

To validate the shape of the  $\text{Fe}_2\text{O}_3$  (used in [24]) particles, additional  $\mu\text{CT}$  data were evaluated. As can be seen in Fig. E.24 for some representative particles, the particles exhibit cavities, and their morphology is generally distinct.

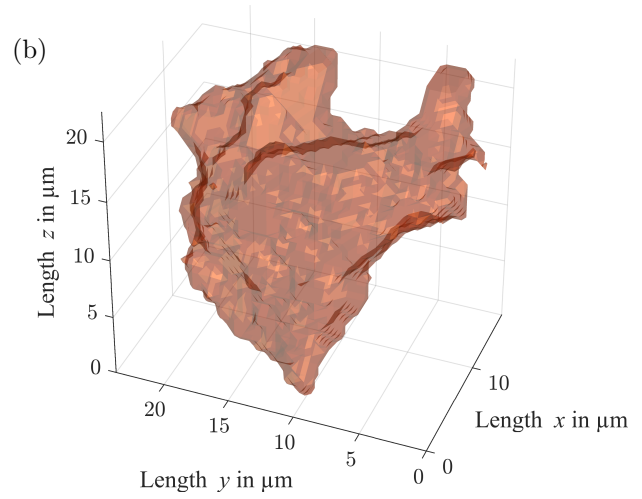
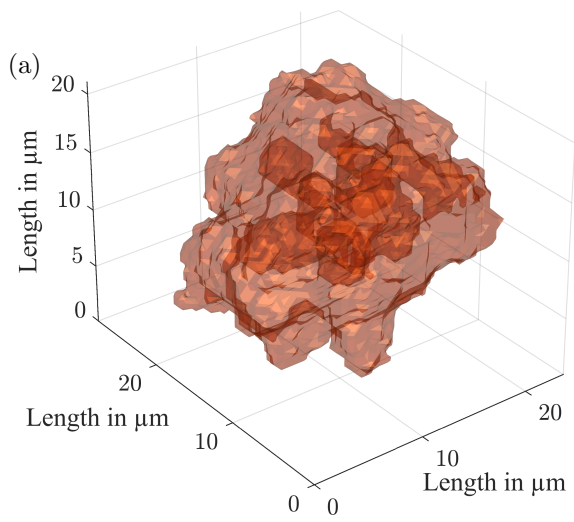


Figure E.24: Reconstructed 3D images from  $\mu\text{CT}$  measurement data [37]:  $\text{Fe}_2\text{O}_3$  particle with hollow structure used for the measurements in [24].